

OPTICAL CONSTANTS FOR  $Y_2O_3$  IN THE EXTREME ULTRAVIOLET

by

Joseph Boone Muhlestein

Submitted to Brigham Young University in partial fulfillment

of graduation requirements for University Honors

Department of Physics and Astronomy

Brigham Young University

February 2009

Advisor: R. Steven Turley

Honors Representative: Bart Kowallis

Signature: \_\_\_\_\_

Signature: \_\_\_\_\_

Copyright © 2009 Joseph Boone Muhlestein

All Rights Reserved

## ABSTRACT

### OPTICAL CONSTANTS FOR $Y_2O_3$ IN THE EXTREME ULTRAVIOLET

Joseph Boone Muhlestein

Department of Physics and Astronomy

Bachelor of Science

The index of refraction of  $Y_2O_3$  has been measured in the extreme ultraviolet region of 5 nm to 30 nm. These measurements demonstrate the potential use of  $Y_2O_3$  as a reflective material in the extreme ultraviolet.  $Y_2O_3$  is also a very stable material in vacuum and in atmosphere which further distinguishes it as a practical choice for an EUV mirror. The sample studied was grown using electron beam evaporation and later heated for 29 hours at 623 °C. This represents the first experimental measurement of  $Y_2O_3$  in this wavelength range and represents an improvement over previous data calculated using atomic scattering factors. Measurements were taken at the Advanced Light Source at the Lawrence Berkeley National Laboratory using Beamline 6.3.2. Previous work done at BYU has shown that an Al/ $Y_2O_3$  multilayer mirror should be effective at maximizing reflectance at 30.4 nm and minimizing reflectance at 58.4 nm, a useful combination for detecting the relatively weak 30.4 nm line of  $He^+$  over the stronger 58.4 nm line of neutral He.

## ACKNOWLEDGMENTS

I would like to especially thank Dr. Turley for all of his work on both the writing and the research behind this thesis. Also all the members of the EUV/Thin Films group that assisted throughout the course of this project. My wife has been a wonderful support allowing me to spend the time necessary to complete this thesis. I would also like to acknowledge the financial support of the Rocky Mountain NASA Space Grant Consortium, the Department of Physics and Astronomy at BYU, and the National Science Foundation via the BYU REU program (Grant # PHY-0552795).

# Contents

<b>1</b>	<b>Introduction</b>	<b>1</b>
1.1	Interest in the Extreme Ultraviolet . . . . .	1
1.2	Project Background . . . . .	2
<b>2</b>	<b>Theory</b>	<b>3</b>
2.1	General Principles of Light and Refraction . . . . .	3
2.1.1	Optical Constants . . . . .	5
2.1.2	Snell's Law . . . . .	8
2.1.3	Electromagnetic Wave Propagation . . . . .	9
2.1.4	Reflection . . . . .	10
2.1.4.1	Polarization . . . . .	11
2.1.4.2	An Example . . . . .	12
2.2	Thin Films . . . . .	12
2.3	CXRO calculations . . . . .	15
<b>3</b>	<b>Experimental</b>	<b>17</b>
3.1	The $\text{Y}_2\text{O}_3$ Sample . . . . .	17
3.1.1	Sample preparation . . . . .	17
3.1.2	Possible contamination . . . . .	18
3.1.3	Sample physical characterization . . . . .	18
3.2	Taking Data at the ALS . . . . .	19
3.2.1	Description of the ALS . . . . .	19
3.2.2	Experimental procedure and error . . . . .	20
3.3	Data normalization . . . . .	23
3.3.1	Raw data . . . . .	23

3.3.2	Measurements . . . . .	23
3.3.2.1	Dark Current . . . . .	24
3.3.2.2	Initial intensity ( $I_0$ ) . . . . .	25
3.3.2.3	Beam Current . . . . .	25
3.3.3	Analysis . . . . .	27
3.4	Fitting . . . . .	28
3.4.1	Model of Film . . . . .	28
3.4.2	Fitting Procedure . . . . .	29
3.4.3	Determining Thickness . . . . .	30
3.4.4	Fitting results and error analysis . . . . .	32
<b>4</b>	<b>Conclusions</b>	<b>35</b>
<b>A</b>	<b>MatLab Code</b>	<b>37</b>
A.1	parratt.m . . . . .	37
A.2	fitfunc.m . . . . .	38
A.3	analyzer4.m . . . . .	39
A.4	filler4.m . . . . .	42
A.5	combiner.m . . . . .	43
A.6	polarfind.m . . . . .	44
A.7	mocastd.m . . . . .	45
A.8	sindx.m sio2ndx.m y2o3.m . . . . .	45

# List of Figures

2.1	Light passing through a glass prism. . . . .	3
2.2	Electric and magnetic fields oscillating in time. . . . .	4
2.3	One wavelength of a sinusoidally varying electric field in arbitrary units. . . . .	5
2.4	The electromagnetic spectrum with the EUV spectrum indicated specifically. . . . .	6
2.5	The electric field of a plane wave as it enters a dielectric material. . . . .	7
2.6	A single ray of light shown reflecting and refracting at an interface. . . . .	8
2.7	Polarization of the ALS synchrotron as a function of wavelength. . . . .	11
2.8	Reflection and refraction off of a thin film. . . . .	13
2.9	Constructive and destructive interference between two waves in phase. . . . .	13
2.10	Diagram of simple multilayer reflector. . . . .	15
3.1	AFM image of the $Y_2O_3$ sample. . . . .	19
3.2	Power spectral density and additional data taken on the AFM. . . . .	20
3.3	Diagram of Beamline 6.3.2 and its various optical components. . . . .	21
3.4	Completely unnormalized data taken at two separate gains. . . . .	23
3.5	Raw data with only the gain normalized. . . . .	24
3.6	Dark current data. . . . .	25
3.7	$I_0$ with no normalization. . . . .	26
3.8	Beam current data shown for both a long and short time scale. . . . .	26
3.9	Good, average, and poor fits obtained during data analysis. . . . .	29
3.10	Results of thickness measurements for nine different wavelengths. . . . .	31
3.11	Real part of the index of refraction plotted against the data given by the CXRO. . . . .	32
3.12	Imaginary part of the index of refraction plotted against the data given by the CXRO. . . . .	33
3.13	A visualization of the various components of error in error-space. . . . .	34

# Chapter 1

## Introduction

### 1.1 Interest in the Extreme Ultraviolet

New applications for extreme ultraviolet (EUV) light, 1–100 nm, have caused an increased interest in the optical properties of materials in the EUV. Advancements in using photo-lithography for the micro-fabrication of electronic components has made the wavelength of light the limiting factor in further minimizing the size of components. By using EUV light, it is possible to put more components onto a single chip, that results in devices which draw less power, produce less heat, and run faster. Many astronomical measurements are also dependent on the EUV. While the sun emits light on its surface in the visible, much of the stellar core emits light in the EUV. Additionally, we can study the earth's magnetosphere by measuring the emission of trapped helium ions which emit radiation in the EUV.

Biological science is also finding use for the EUV as a means of imaging proteins and other subcellular structures. Visible microscopy becomes unclear as the magnification is extended, while electron microscopes require extensive preparation which destroys the natural organic environment. This can destroy the structure of the intricately folded protein and thus loses much of the important data. EUV microscopy provides a useful intermediary that can extract more data from the sample than electron microscopy while obtaining higher magnifications than would be possible with visible light. These and other applications make accurate measurement and manipulation of EUV light an emerging area of interest among scientists.



## 1.2 Project Background

Yttrium oxide became an element of interest in 1999 as a result of work done by Shannon Lunt[6]. Lunt and the BYU EUV/Thin Films Group were working to develop a mirror for the IMAGE mission NASA was preparing to launch. The requirements for the mirror were that it maximize reflection at 30.4 nm where singly-ionized helium emits most brightly in the earth's magnetosphere and minimize reflection at 58.4 nm, the prominent emission line of neutral helium found in the ionosphere. She developed a genetic algorithm which would calculate reflectance for various multilayer mirrors to find the most advantageous combination possible. Her results indicated that a mirror with alternating layers of aluminum and yttrium oxide would best fulfill the given requirements.

While Lunt's results indicated that yttrium oxide had potential to make an excellent EUV mirror, uncertainty in the index of refraction for yttrium oxide and difficulty in fabricating the yttrium oxide/aluminum mirrors prevented the group from using this material combination for the IMAGE mirror. The best index data that she had available to her in the applicable wavelength region came from the Center for X-Ray Optics (CXRO) at the Lawrence Berkeley National Laboratory, and used atomic scattering factors to calculate the index[3, 4, 5]. No direct measurements had been taken.

An additional area of interest for yttrium oxide lies in its chemistry. Since yttrium oxide ( $Y_2O_3$ ) is already oxidized, it is more stable than a pure element in the oxygen-rich atmosphere and will not develop a surface oxide layer that can change its optical properties. It is also an extremely stable oxide, often leaching oxygen away from adjacent oxygen containing layers such as  $SiO_2$ . It is also an inexpensive, non-hazardous material that can be obtained easily.

The advantageous properties Lunt calculated for  $Y_2O_3$  surprised the group. The conventional wisdom concerning compounds in the EUV was that pure elements would affect the light individually such that a mixture would give an intermediate effect. While this is still not completely understood, it is clear that the chemical composition of the compound acts differently than the isolated atomic materials. As I'll show later, there is appreciable difference between the experimental results I have measured and the data which assumes each element is independent in its effect.

# Chapter 2

## Theory

### 2.1 General Principles of Light and Refraction

The study of optical constants begins with a simple physical observation: when light enters a medium (such as glass, air, or anything else transparent) it bends. This phenomenon is what allows our eyes, glasses, and telescopes to magnify and focus images. When we look at a prism, we notice another important phenomenon: not all light bends the same amount. This is why the colors in light separate into a rainbow when we put them through a simple prism (see Figure 2.1).

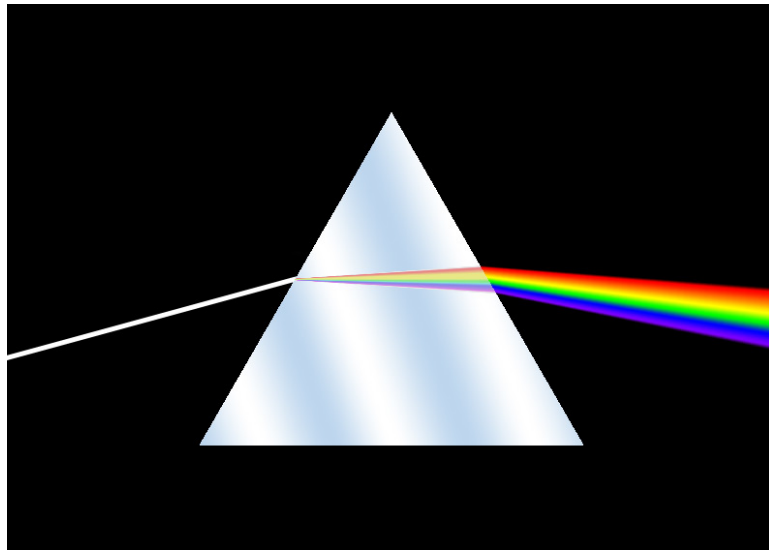


Figure 2.1: This illustrates visible light passing through a glass prism and how it affects each wavelength (or color) differently [2].

What is unique about the various colors of light that makes glass affect them differently? To answer this, we must understand that light is made up of waves of electric and magnetic fields oscillating in time and space. An example of this is shown in Figure 2.2 where one can see the electric field represented by the flat waves and the magnetic field represented by the vertical waves.

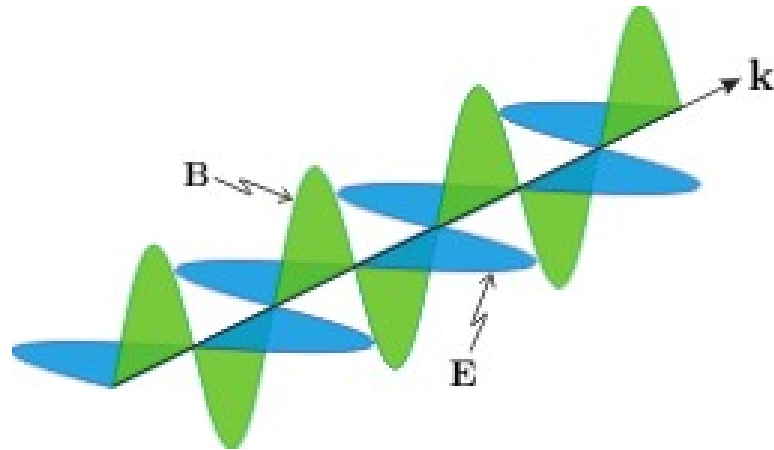


Figure 2.2: This diagram shows electric (E) and magnetic (B) waves propagating in the  $k$  direction [1]. (used with permission)

Different colors are created by light of different wavelengths. If a wave were frozen in time, the wavelength would be how far one would need to measure to go through one entire oscillation. This can also be thought of as the distance from one peak to the next peak. Figure 2.3 illustrates a single wavelength.

The wavelength of light can vary dramatically. Radio waves from an AM radio can have a wavelength several meters long. Gamma rays can have wavelengths of less than one trillionth ( $10^{-12}$ ) of a meter, or a picometer. Visible light ranges in wavelength from about 380 nm (nanometers or  $10^{-9}$  meters) to 750 nm. All of these are examples of the same electromagnetic waves but can behave very differently. Figure 2.4 shows the electromagnetic spectrum and approximate wavelength regimes for different types of waves.

With this understanding of wavelengths we are ready to look back to the prism example. The reason that different colors bend differently in a material is because each color has a unique wavelength and each wavelength reacts differently with the material. To predict how a certain wavelength will be affected by a certain material, we will need to know about two new concepts, optical constants and Snell's law.

Later in this chapter, I will also will also discuss mathematically the theory behind electromagnetic wave propagation. This will allow me to finally apply the various concepts to thin film reflectors

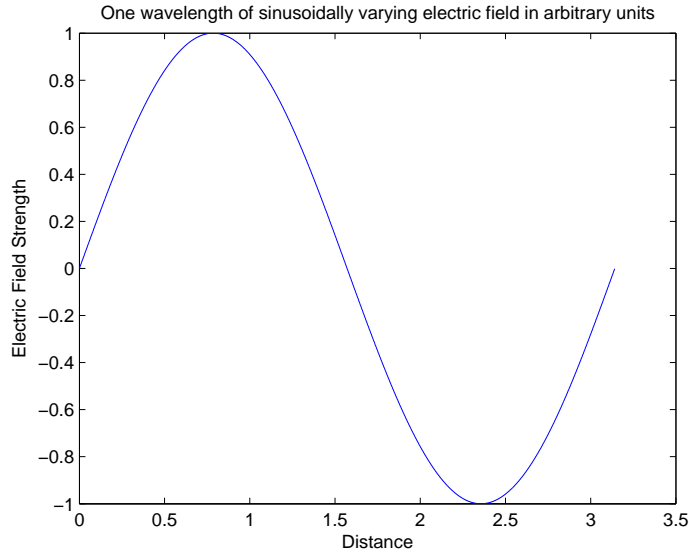


Figure 2.3: This figure illustrates a single wavelength of an oscillating electric field wave. The magnetic field wave would have the same wavelength but be perpendicular to this one as shown in Figure 2.2.

and explain the theoretical model we used in fitting the optical constants.

### 2.1.1 Optical Constants

When light, an electromagnetic wave, enters a material, it begins to interact with the atoms of that material. This interaction will often slow the propagation of the wave, but it may also speed it up. It may absorb some of the energy of the wave, or, as in the case of a laser (*Light Amplification by Stimulated Emission of Radiation*) it may amplify light. Each of these effects, velocity and amplification/absorption, can be characterized by a number known as an index of refraction.

In the case of the velocity, the real part of the index of refraction  $n$  is inversely proportional to the phase velocity of the wave in a vacuum. For example, if a material has an index of refraction of two, then the light will travel at one half the velocity of light in vacuum. If the  $n$  is less than one, the velocity will be faster than light in vacuum. However, an interface which has an  $n$  less than one must also have a  $k$  which is not-zero. This interface will attenuate the light. Light that is attenuated is a combination of waves with different wavelengths. While the speed of an individual wave might exceed the speed of light in the vacuum, the speed of the combined wave will be less than the speed of light. For further explanation on this phenomenon, please see [1], Chapter 7, especially 7.6.

In the case of amplification/absorption, the constant  $k$  describes how rapidly the amplitude or

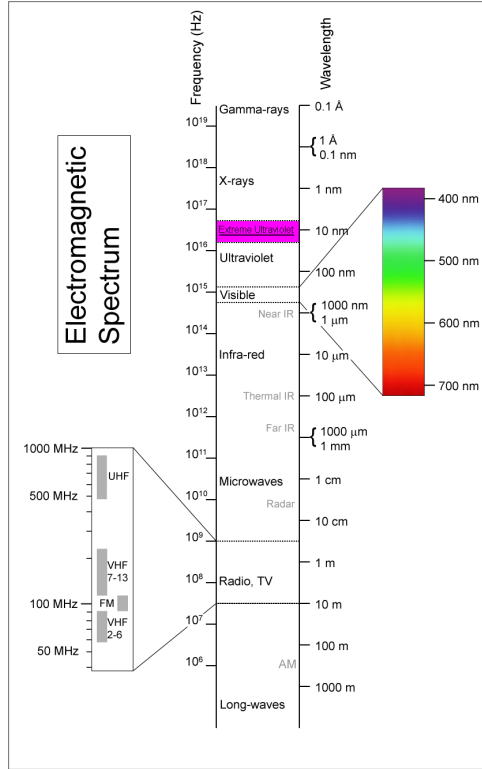


Figure 2.4: This shows the visible spectrum and where it falls within the greater electromagnetic spectrum. Shown in fuchsia is the EUV spectrum [8].

strength of the light is absorbed by the material. For vacuum where no energy is lost or gained,  $k$  will be zero. A material that absorbs energy as the light propagates will have a positive  $k$  while a material that amplifies the light will have a negative  $k$ .

These two constants are known as the real ( $n$ ) and imaginary ( $k$ ) parts of the index of refraction. Often they are written as a single complex number  $N = n + ik$ . This is useful as it allows both constants to be applied simultaneously in an equation using complex notation. An example of the usefulness of this notation is given by Peatross and Ware in Chapter 2 [1]. They first derive the expression for a plane wave:

$$\mathbf{E}(\mathbf{r}, t) = \mathbf{E}_0 e^{i(\tilde{\mathbf{k}} \cdot \mathbf{r} - \omega t)} \quad (2.1)$$

However, this expression for a plane wave is unique to vacuum. One way to tell is that  $n$  and  $k$  are not represented. The  $\tilde{\mathbf{k}}$  in the equation is a vector defined as  $\tilde{\mathbf{k}} \equiv \frac{2\pi}{\lambda_0} \hat{\mathbf{k}}$  with  $\hat{\mathbf{k}}$  representing a unit vector in the direction of the wave's propagation, the vector  $\mathbf{r}$  representing a position in three dimensional space,  $\omega$  defined as  $\omega \equiv \frac{2\pi c}{\lambda_0}$ , and  $c$  being the speed of light,  $2.9979 \times 10^8 \text{ m/s}$ . It is noted that this formula has hidden the phase information of the wave in the complex coefficient,  $\mathbf{E}_0$ , and that the real part alone holds physical significance. If we want to extend our description of a plane

wave to a material, a dielectric like  $\text{Y}_2\text{O}_3$  for example, we must include information specific to that material. Peatross and Ware continue their derivation for the case of a dielectric and come to the expanded formula (again, just looking at the real part):

$$\mathbf{E}(\mathbf{r}, t) = \mathbf{E}_0 e^{-\frac{k\omega}{c} \hat{\mathbf{k}} \cdot \mathbf{r}} e^{i(\frac{n\omega}{c} \hat{\mathbf{k}} \cdot \mathbf{r} - \omega t)} \quad (2.2)$$

$k$  is here seen in the decaying exponential term while  $n$  is contained within the complex exponential (a cos when the real part is taken). Figure 2.5 shows equation 2.2 plotted for  $k = 0.1$ ,  $n = 2$ .

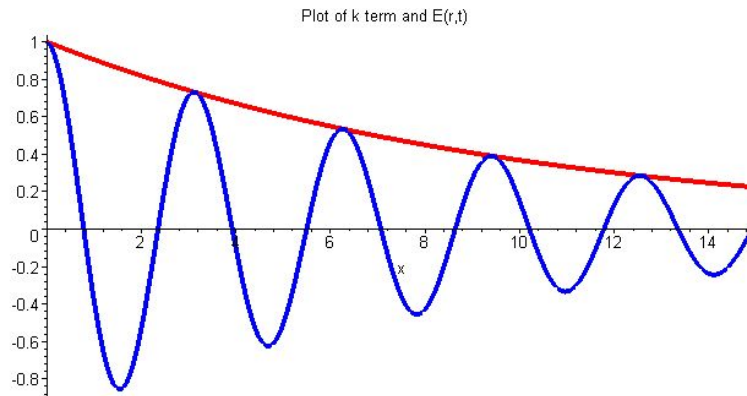


Figure 2.5: The electric field of a plane wave as it enters a dielectric medium (blue) and the corresponding decaying exponential (the term in equation 2.2 that contains  $k$  - red). As only the real part of Equation 2.2 has physical significance, it is also the only part of the equation plotted here. The scale is dimensionless,  $k = 0.1$ , and  $n = 2$ .

One other important aspect about optical constants is how they are determined. The constants are unique for each material and for each wavelength of light propagating through that material. Since there are many different materials and wavelengths, many optical constants have yet to be determined experimentally. Various methods have been derived to determine these constants theoretically and while such methods are useful, they are not as reliable as experimentally measured constants.

It is also important to realize the relationship between the electric field described by the equations above and the signal that we can experimentally measure. Our measurements detect the intensity ( $I$ ) of the light. Intensity is proportional to the square of the magnitude of the electric field, or  $I \propto |\mathbf{E}(\mathbf{r}, t)|^2$ .

### 2.1.2 Snell's Law

Willebrord Snellius was a Dutch physicist and mathematician who is credited for being the first to describe the relationship of the angles of light going into and out of a material. He discovered that if he measured the angle of light entering a material with normal incidence (perpendicular to the material) and the angle of light within the material with normal incidence, the sine's of these two angles would be proportional (See Figure 2.6). Using the index of refraction, Snellius turned

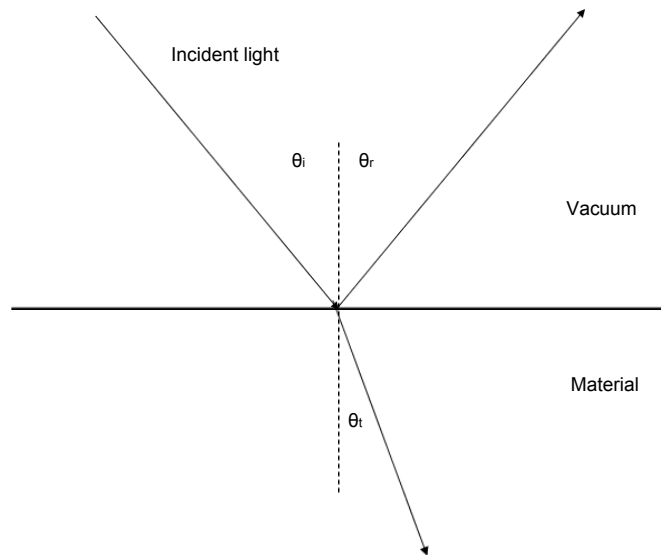


Figure 2.6: Diagram of light incident on a surface such as glass and the reflected and refracted rays. Note that  $\theta_i = \theta_r$ .

this proportionality into an equality:

$$n_i \sin(\theta_i) = n_t \sin(\theta_t) \quad (2.3)$$

This is the typical form of Snell's law. Note that  $n_i$  and  $n_t$  refer just to the real part of the index of refraction. This law allows us to finally understand the prism example. As each color interacts with the glass, it is bent according to Snell's law. Since each wavelength has a different optical constant  $n$  for its interaction with the glass, the angle by which it refracts will be different as well. This is true for all electromagnetic radiation propagating through any material. This includes my area of interest of EUV light interacting with yttrium oxide.

### 2.1.3 Electromagnetic Wave Propagation

Waves are formed when an event at one time and place affects something in an adjacent time and place. With ripples in a pond, a pebble dropped in only affects the water it contacts. This water proceeds to affect subsequent water particles causing the effect to propagate outward. A very similar phenomenon is present with sound which has air particles moving air particles as the wave moves along. These are both mechanical wave types since they involve a mechanical interaction (the collision of molecules) which is the mechanism for propagation.

Similar to mechanical waves such as in water and air, light waves are caused by an event at a specific time and place affecting something in a neighboring time and space. With light waves, however, it is a change in the electric or magnetic field which is the mechanism of propagation meaning that no substance is necessary for the wave to continue. This is understood in modern optical theory through the use of two of Maxwell's equations:

$$\nabla \times \mathbf{E} = -\frac{\partial \mathbf{B}}{\partial t} \quad (\text{Faraday's Law}) \quad (2.4)$$

$$\nabla \times \frac{\mathbf{B}}{\mu_0} = \epsilon_0 \frac{\partial \mathbf{E}}{\partial t} + \mathbf{J} \quad (\text{Ampere/Maxwell Law}) \quad (2.5)$$

Faraday's law tells us that the curl of the electric field is equal to the change in the magnetic field. This is illustrated by a generator which uses mechanical power (like a windmill or diesel engine) to spin a magnet inside of a loop of wire and produce an electrical current. The spinning magnet causes the magnetic field within the loop of wire to change with time ( $-\frac{\partial \mathbf{B}}{\partial t} \neq 0$ ). When this right hand side term of Faraday's law is no longer zero, then the left hand side ( $\nabla \times \mathbf{E}$ ) is also not zero. In non-mathematical terms, this means that an electric field is created in the vicinity of the spinning magnet which in turn causes a current to form within the wire. It is important to realize that the field is created even if there is no wire to conduct a current.

Ampere's law, which was later revised by Maxwell, describes the opposite case of Faraday's law, that change in electric field can create a new magnetic field. The  $\mathbf{J}$  refers to a current that can create a magnetic field and can generally be ignored for our study of light in vacuum. Similar to Faraday's law, the  $\epsilon_0 \frac{\partial \mathbf{E}}{\partial t}$  term refers to a change in electric field. The equation shows us that a magnetic field will be created in the presence of such a changing electric field.

The important message from these two equations is that a change in magnetic field will cause an electric field to form, and that a change in electric field will cause a corresponding magnetic field to form. This interplay of electric and magnetic fields provides the necessary interaction for the wave to



propagate. Since this propagation doesn't involve the interaction of matter on matter, it is possible for light to pass through vacuum where mechanical waves are unable to exist. Matter, composed of charged protons and electrons, interacts with these fields. This leads to the various effects discussed in section 2.1.1 and described by the optical constants  $n$  and  $k$ . It is also from these equations that equations 2.1 and 2.2 are derived.

### 2.1.4 Reflection

The phenomenon of reflection grows out of the discussion of electromagnetic waves and optical constants. When a wave passes from one medium into another, the wave must alter itself to continue passing through the new medium. One change is the change in phase velocity that we looked at in relation to the optical constant  $n$ . Another important change is that in order to pass into the new medium, it is possible that some of the energy in the wave will need to be discarded. As the energy can't simply disappear, it is instead reflected off the interface. The amount that the light is reflected will be determined by both the index of refraction of the two materials at the interface and the angle with which the wave is incident on the interface.

Augustine Fresnel realized this phenomenon and was able to quantify the amount of light that would reflect or transmit at an interface. His results, known now as the Fresnel coefficients, are a direct result of Maxwell's equations and provide a starting point for most discussions of electromagnetic waves interacting with an interface. Peatross and Ware provide a derivation of these coefficients on pages 63-65 of their textbook [1].

$$r_s = \frac{n_i \cos \theta_i - n_t \cos \theta_t}{n_i \cos \theta_i + n_t \cos \theta_t} \quad (2.6)$$

$$r_p = \frac{n_i \cos \theta_t - n_t \cos \theta_i}{n_i \cos \theta_t + n_t \cos \theta_i} \quad (2.7)$$

$$t_s = \frac{2n_i \cos \theta_i}{n_i \cos \theta_i + n_t \cos \theta_t} \quad (2.8)$$

$$t_p = \frac{2n_i \cos \theta_i}{n_i \cos \theta_t + n_t \cos \theta_i} \quad (2.9)$$

Here  $r$  represents the ratio of the reflected electric field ( $E_r$ ) to the incident electric field ( $E_i$ ),  $r = \frac{E_r}{E_i}$ , with  $t$  similarly defined for the transmitted field ( $E_t$ ),  $t = \frac{E_t}{E_i}$ . The  $s$  and  $p$  subscripts refer to the polarization which will be discussed in Section 2.1.4.1. These equations were derived with  $\theta$  measured from normal incidence. As calculations in the EUV are typically done with  $\theta$  measured from grazing, they can be used with the substitution  $\theta_{EUV} = \pi - \theta$ .

### 2.1.4.1 Polarization

One important thing that Fresnel's results teach us is that there is a difference between waves that have their electric fields oscillating parallel or perpendicular to the plane containing both the incident beam and the reflected beam. Referring to Figure 2.6, the electric field can either oscillate parallel to the image or perpendicular to it (in and out of the page). This orientation is known as polarization and has an important effect on reflection and refraction. Fresnel realized this and has separate coefficients for each polarization. Common notation to differentiate them uses the subscripts 's' and 'p' which respectively stand for perpendicular and parallel. This convention comes from the German translations of the words senkrecht and parallel respectively.

The polarization of the light at the ALS is wavelength. In private correspondence with Eric Gullikson we obtained a graph of this dependence. This data was digitized by photographing the graph, using a mouse to mark several points along the curve, and interpolating between the points using a cubic spline. The data used in our fits is given in Figure 2.7 as a function of wavelength ( $\lambda$ ). The code used to calculate this polarization is available in Section A.6. It is also noted that Eric

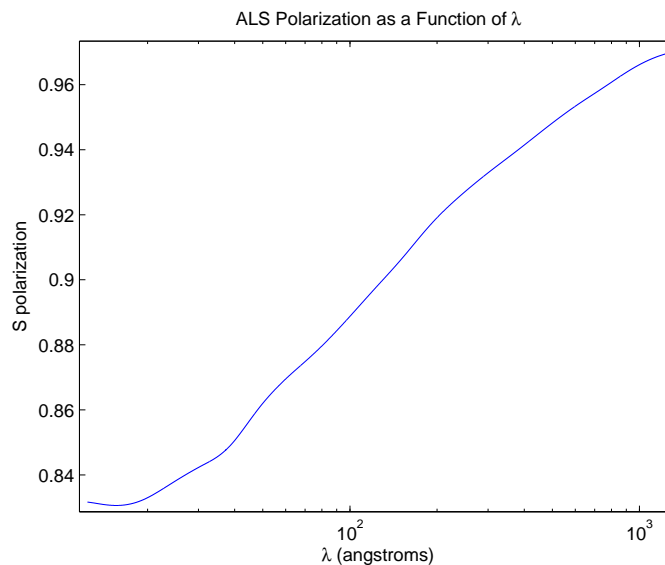


Figure 2.7: Polarization of the ALS synchrotron as a function of wavelength. This is a digitized version of data provided by Eric Gullikson.

Gullikson has measured the polarization at two unique wavelengths and found the results to be in approximate agreement with the data on the graph.

### 2.1.4.2 An Example

One way to imagine how a wave can partially reflect and partially transmit is to consider a mechanical wave. A rope that you pull up and then down quickly to create a pulse wave can serve as the example. If the rope is uniform, then the wave pulse will continue until friction steals all of its energy. However, if the rope is tied to a wall, then the pulse will all come back. If you were to perform this experiment and observe closely, you would also notice that the pulse would flip upside down. This phenomenon, known as a phase shift will be important later.

Both of the above cases show extremes of an interface. One allows all the energy to pass by having no change, while the other allows no energy to pass by having a very (essentially infinite) change. At most interfaces light encounters, it will experience something in the middle. This could be described, using the rope example, as a change in the rope from a small rope to a much larger rope. If you were to perform this experiment, you would see the wave pulse continue on in the thicker rope, but it would be much smaller than in the rope that stayed the same size.. You would also see a second wave pulse reflect back much like the case of the rope attached to the wall. This wave would also be smaller than the corresponding extreme case, but it would also exhibit the phase shift of being flipped upside down.

Interestingly, if you started with the thick rope and watched it transmit to a thin rope, you would not see this phase shift. This translates very easily into light waves. If light reflects off of a high index of refraction from a low one, say light in air reflecting off of glass, the light will experience a phase shift of  $180^\circ$ . If the light is in glass and bounces off the interface with air, it will not have a phase shift.

## 2.2 Thin Films

Thin films give an added layer of complexity to the reflection of light off of a material. Light reflects off of both the top and bottom layers resulting in two distinct paths the light can travel before leaving the surface as shown in Figure 2.8. While the direction of the two waves is identical (both leave at an angle  $\theta_r$  from the surface), their phase could be different. (Recall Figure 2.3. The light can be at a maximum, minimum, or somewhere in between. Also, recall the possible phase shift we saw with the rope example. This can affect whether the interference adds or takes away from the final waves amplitude.) This leads to either constructive or destructive interference. If the two waves are in phase, they will constructively interfere and produce a single wave that is twice as

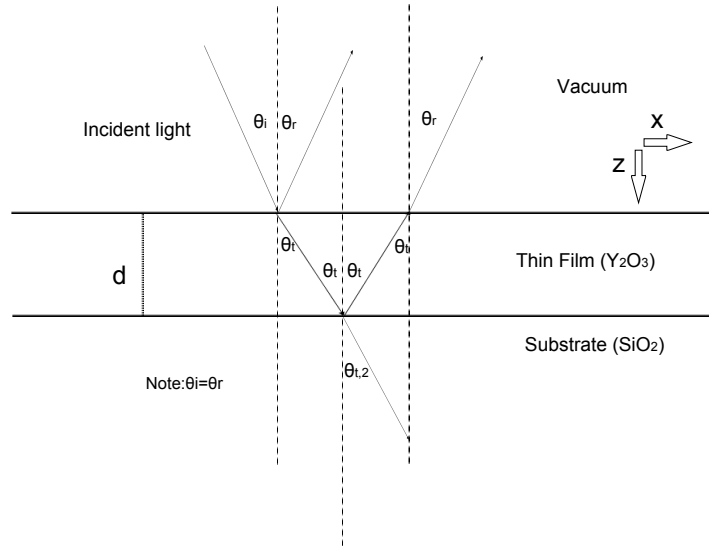


Figure 2.8: Diagram of thin film reflection pattern. Materials in parenthesis are specific to my experiment.

strong as either initial wave (see Figure 2.9 ). If they are one half wavelength out of phase, they

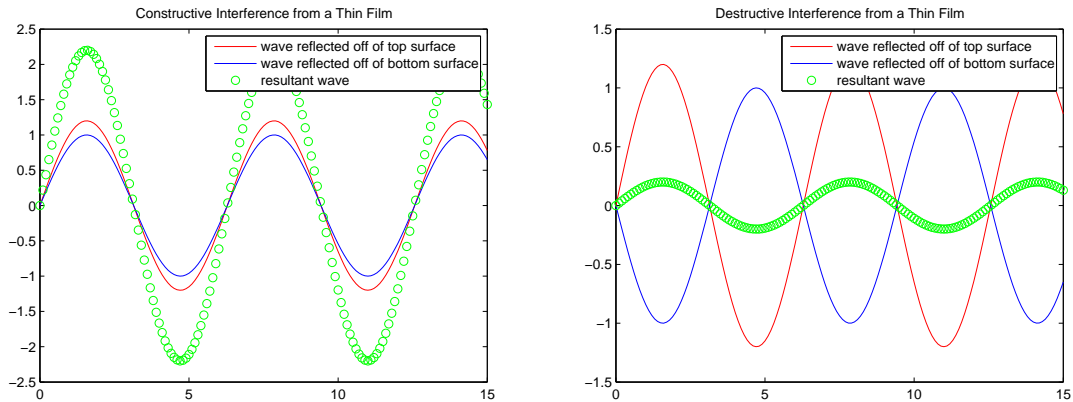


Figure 2.9: Constructive and destructive interference between two waves in phase. Notice the large amplitude of the resultant wave in the constructive case and the small amplitude of the resultant wave in the destructive case.

will destructively interfere and cause less light to reflect than either wave on its own. The type of interference that occurs is a function of three things: the wavelength of the light, the thickness of the film, and the materials used (their index of refraction).

A multilayer mirror is just a thin film mirror that has multiple layers. Since each interface will reflect a certain amount of the light that hits it, added layers can greatly increase the potential reflectance by increasing the number of interfaces. The quantitative analysis of multilayer films can

be found at [1]. Finding the theoretical reflectance of EUV light off of thin film mirrors is also an integral part of fitting the data I have collected. The Parratt formula was developed to specifically treat EUV radiation as it interacts with a multilayer reflector. This takes into account the reflection which arises from each of multiple interfaces to calculate the composite effect on reflection. I used a variant of the original Parratt formula [7] which is described on pages 11-14 of [6]. My code is also available in Section A.1 of Appendix A. The goal is to find  $R_n$ , the ratio of the reflected light by the total light, using the equation:

$$\mathbf{R} = |R_n|^2 \quad (2.10)$$

The basic formula, as stated by Lunt, is:

$$R'_2 = \frac{C_2^4(r_{21} + R'_1)}{1 + r_{21}R'_1} \quad (2.11)$$

where

$$R'_m = C^2 R_m \quad (2.12)$$

and  $C$  is the phase after transmitting half way through a layer.  $C$  is given by:

$$C = e^{\frac{ik_z d}{2}} \quad (2.13)$$

where

$$k_z = \frac{2\pi}{\lambda_0} \sqrt{n^2 - \cos^2 \theta} \quad (2.14)$$

and  $r_{21}$  refers to the Fresnel coefficient particular to the 2→1 interface as shown in Figure 2.10 (Equation 2.6 for s polarization and Equation 2.7 for p polarization). The direction  $\hat{z}$  referenced by  $k_z$  is as shown in Figure 2.10. As can be seen in the formula,  $R'_2$  is found based on the phase, Fresnel coefficients, and the  $R'$  from the previous layer. The formula is thus recursive and can be used for many layers by incrementing the subscripts on the various factors. We also note that  $R'_1$  will be zero as the bottom layer will only transmit, so there is no reflectance. (Were there any reflectance measurable, we would need to count this layer as the 2<sup>nd</sup> to bottom layer and count what the light is reflecting off of as the bottom layer.) This gives us a starting point from which to begin the recursion formula. As there is a unique  $r$  for each polarization, we also may extend this analysis to each of the polarizations separately and combine them proportionally at the end. This may done

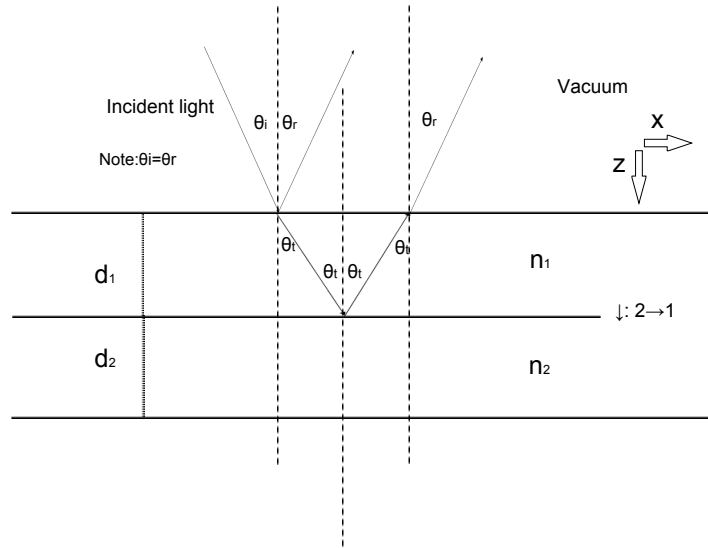


Figure 2.10: Diagram of simple multilayer reflector.

if we know the fraction of the light that is polarized  $s$  ( $f_s$ ) and  $p$  ( $f_p$ ) as follows:

$$R = f_s |r_s|^2 + f_p |r_p|^2 \quad (2.15)$$

## 2.3 CXRO calculations

The Center for X-Ray Optics (CXRO) website gives an excellent primer on the way that they use atomic scattering factors to estimate the index of refraction for materials in the EUV [4]. Due to its relevance to my project, I will summarize their discussion here.

They start with the atomic scattering factors for an element,  $f = f_1 + if_2$ , which are unique to each element and each wavelength combination. They then give equations for  $\delta$  and  $\beta$  which relate to  $n$  and  $k$  according to  $n = 1 - \delta$  and  $k = \beta$ :

$$\delta = \frac{1}{2\pi} N r_0 \lambda^2 f_1 \quad (2.16)$$

$$\beta = \frac{1}{2\pi} N r_0 \lambda^2 f_2 \quad (2.17)$$

where  $r_0$  is the classical electron radius ( $2.81794 \times 10^{-15}$  m),  $\lambda$  is the wavelength, and  $N$  is the

atomic density of the material. In the case of a compound such as  $Y_2O_3$ , it is necessary to take a weighted average of the component elements. As there will be two yttrium atoms for every three oxygen atoms, the data for  $Y_2O_3$  would be:

$$\delta_{Y_2O_3} = \frac{2}{5}\delta_Y + \frac{3}{5}\delta_O \quad (2.18)$$

$$\beta_{Y_2O_3} = \frac{2}{5}\beta_Y + \frac{3}{5}\beta_O \quad (2.19)$$

It should also be noted that this approximation is only valid when the energy of the incident photons are far removed from the absorption edge of the element or compound. This is the case in the region studied for this project.

## Chapter 3

# Experimental

### 3.1 The $\text{Y}_2\text{O}_3$ Sample

#### 3.1.1 Sample preparation

The sample we made measurements on was made by Anthony Willey and David Allred in the lab of Matthew Linford. Analytical grade  $\text{Y}_2\text{O}_3$  chunks provided by Allred were evaporated with a 5 keV beam with the current not exceeding 40 A. The  $\text{Y}_2\text{O}_3$  for deposition was held in a graphite crucible and some black residual was seen on the surface as evidence of melting. The Si/SiO<sub>2</sub> sample wafer was located on a plastic compact disc blank approximately 50 cm above the  $\text{Y}_2\text{O}_3$  which rotated on the axis of the disc and revolved at a radius of 10 cm about the center line above the deposition material. The blank was set at a 45° angle toward the  $\text{Y}_2\text{O}_3$  below.

After deposition, the sample was cleaned using an excimer UV lamp by Elisabeth Strein. After the treatment, Allred visually inspected the sample and reported that the interference pattern off the surface of the material had noticeably been altered. Willey and Allred proceeded to thermally treat the sample to try and remove any impurities which may have occurred during the deposition process. They heated the sample in a Lindbergh Furnace for 29 hours and at a temperature of 623°C. Ellipsometry data was taken on the sample before and after the thermal treatment and a reduction in thickness of approximately 30% was observed.



### 3.1.2 Possible contamination

During deposition, the cold trap associated with the oil diffusion vacuum pump ran out of liquid nitrogen several times presenting a possible source of contamination. The oil contains both silica ( $\text{SiO}_2$ ) and carbon and is a likely source for the impurities targeted by the heat treatment. It is expected that the carbon would have been removed through the baking process though the silicon would have been left. David Allred subsequently took ellipsometry data of the sample and found that adding a 26% silica content to the sample greatly improved the quality of the fit.

This ellipsometry data is questionable, however, as a separate sample deposited by sputtering and on a different vacuum system was also found to be fit much better by adding a 20% silica content. As it is unlikely the two deposition methods would both result in such large amounts of silicon contamination, it is likely another explanation exists. One possible explanation is that the model used for  $\text{Y}_2\text{O}_3$  is unreliable as discussed below in Section 3.1.3.

As shown in Section 3.4.4, the index of refraction measured with the sample correspond closely to the expected data from the CXRO. While contamination remains a possibility, this correspondence, along with the separate samples showing similar properties in the ellipsometry analysis suggest that the sample may not have large impurities.

Using x-ray photoelectron spectroscopy, David Allred, Anthony Willey, and Elisabeth Strein found no evidence of silica contamination on the surface of either sample. This evidence makes silica contamination very unlikely.

### 3.1.3 Sample physical characterization

The finished sample was analyzed by Elisabeth Strein using the ellipsometer in Linford's lab. She determined that the thickness was approximately 20 nm. She did cite concerns in the model used for the calculations and noted a larger error on the results than she typically observed on silicon and silicon dioxide samples which have a well defined model. Error was estimated at 10%. This thickness would later be corroborated by reflection data used in my analysis of the optical constants (see subsection 3.4.3 below). She and Willey also analyzed the data using x-ray photoelectron spectroscopy and found evidence of yttrium, oxygen, and carbon. They were unable to determine accurate ratios. They also were not expecting silicon content at the time and so did not explore the possibility of silicon contamination discussed in Section 3.1.2.

While we have shown that the sample does contain carbon, the group feels that as a result of the thickness change during the temperature treatment, it is likely that most of the carbon contamination

has been removed from the film. The measured carbon would then be adventitious carbon unique to the surface.

With the help of Robert Davis's AFM lab at BYU, Willey characterized the surface roughness with atomic force microscopy. He found it had an RMS roughness of 0.637 nm with a variation in height of 10.1 nm over a  $1\ \mu\text{m}$  square grid. Figure 3.1 is from this AFM analysis. Figure 3.2 shows

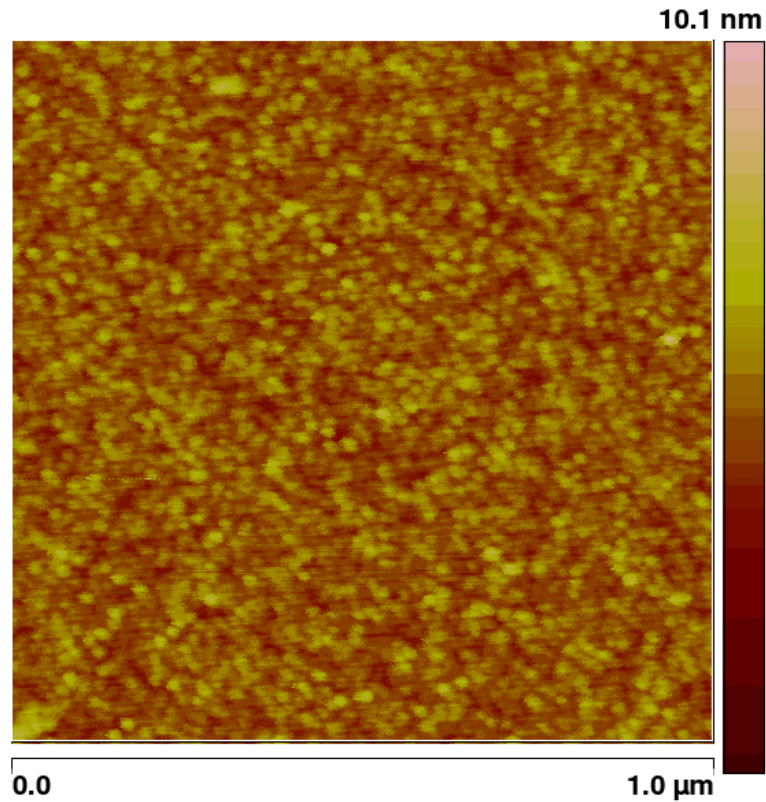


Figure 3.1: AFM image taken by Anthony Willey. The RMS roughness for this sample was calculated to be 0.637 nm.

the power spectral density for the AFM data as well as some additional information.

## 3.2 Taking Data at the ALS

### 3.2.1 Description of the ALS

The Advanced Light Source (ALS) is a third-generation synchrotron located at the Lawrence Berkeley National Laboratory in Berkeley, California. It produces light by accelerating electrons to near the speed of light and confining them within a storage ring. Within the ring, each electron

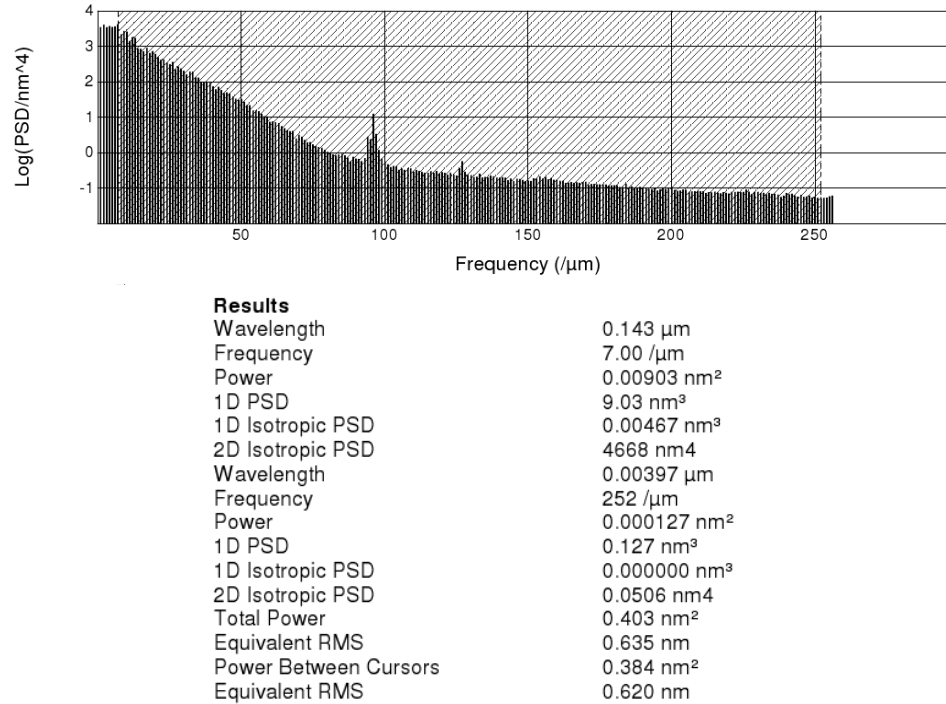


Figure 3.2: Above is plotted the power spectral density for the AFM data taken by Willey. Below is additional data collected by the AFM.

has a nominal energy of 1.9 GeV and is confined to a path approximately the size of a human hair (approximately  $0.20 \text{ mm} \times 0.02 \text{ mm}$ ). The maximum operating current is 400 mA. As the electrons travel around the storage ring, they encounter bend magnets. Each of these is a magnet which causes the trajectory of the electrons to curve. This allows the electrons to keep within the storage ring and also provides a bright source of radiation throughout the EUV spectrum. The brightness,  $10^{15} \text{ photons/sec/mm}^2/\text{mrad}^2/0.1\% \text{ Band Width}$ , produced by such a bend magnet is approximately 100,000 times the brightness of the sun [9].

### 3.2.2 Experimental procedure and error

We used Beamline 6.3.2 at the ALS to take our data (see Figure 3.3). Once the light is created at the bend magnet, it reflects off of a focusing mirror which increases the intensity of the final beam of light. It then passes over one of three blazed diffraction gratings (300, 600, or 1200 lines/mm) to separate the beam into individual wavelengths [11].

The light then passes over another focusing mirror and an order suppressor which reduces second and third order peaks of different wavelengths. However, for wavelengths longer than about 25 nm,

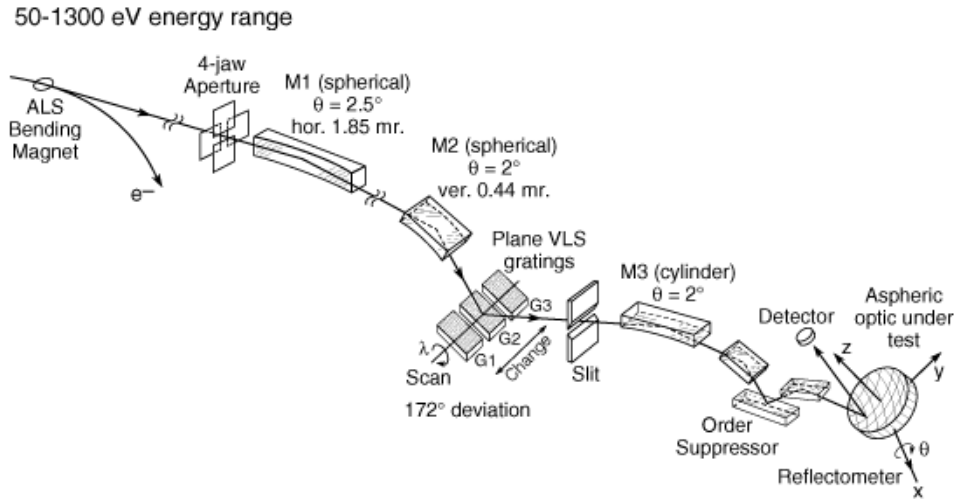


Figure 3.3: Depiction of the relevant optical components of Beamline 6.3.2 at the Advanced Light Source. This beamline was used to take all our measurements [11].

there has been some cause to worry if these higher order wavelengths are being completely suppressed. In comparison with data taken at BYU at 30.4 nm and 58.4 nm it is clear that there are discrepancies within the data. Further, the data I have analyzed and is presented in Figures 3.11 and 3.12 show a much lower confidence level beginning around 25 nm. Finally, as the filter must be adjusted to isolate different wavelength ranges, we would expect that where the ranges overlap would give similar data. Our experience has been that beginning above 25 nm, there is less agreement in the overlap region between the different filter settings (see Figures 3.11 and 3.12).

When the light finally enters the sampling chamber it has very high spectral resolution and purity. The CXRO website reports that the final resolving power ( $\frac{\lambda}{\Delta\lambda}$ ) is 7000 with a photon flux of  $10^{11}$  photons/sec/0.01% Band Width at 100 eV. The reported spot size at the sample is (in  $\mu\text{m}$ ) 10x300 (vertical by horizontal). Polarity is approximately 90% S character [10]. See Section 2.1.4.1 for further discussion on the polarization of Beamline 6.3.2.

The  $\text{Y}_2\text{O}_3$  mirror is placed in the sampling chamber where it can be exposed to the incoming light. Using a LabView-based program known as Metro, we had control of the angle of the detector and the sample stage and the translational movements of the sample stage. We also could control the wavelength of the beam by adjusting the angle of the diffraction grating.

After aligning the system, we took reflectance measurements as a function of angle ( $\theta$ ). We first selected a single wavelength of interest by adjusting the position of the diffraction grating. We would then rotate the sample through the desired angle  $\theta$  and the detector arm by an angle  $2\theta$ . The sample stage is able to be positioned to within 10  $\mu\text{m}$  translationally and to within  $0.002^\circ$

rotationally. However, with the angular divergence of the beam the angular resolution is not as precise. The intensity of the reflected light was recorded at set intervals and saved to the Metro system. We used a gallium arsenide detector which was approximately 1 cm square. The size of the detector allowed us to integrate over a larger spot caused by roughness on the sample surface and offset any slight misalignment in the detector arm and sample stage.

The analog signal from the detector fed through a wire on the detector arm, out of the sampling chamber, and into an amplifier and analog to digital converter. We noticed at times that the system would record additional dark current if we moved the detector arm during the reading. This led us to suspect potential interference in the wire running from the detector to the amplifier. The digitized signal would then cover about thirty feet of wire to the computer which would record the data for analysis.

The amplifier is another source of concern for our data. We controlled the amplification in powers of ten by setting the “gain.” The gain is the amount of amplification that is done before the computer reads in the detector signal. Since the data can change by several orders of magnitude over the scan, it can also be necessary to use a different gain at different parts of the scan. We set the gain manually for each run and the computer records our settings as a power of 10. For example, a gain of 8 means that the voltage from the detector is amplified by a factor of  $10^8$  before it is read in by the computer (see Figure 3.5).

As our controls are limited to setting an integer value, it is difficult to know if the actual amplification is linear as we would expect. This concern has been heightened since some of our data containing data at multiple gains has shown some discrepancies where the amplification has been switched. These discrepancies have not been large as shown in Figure 3.5. Finally, the noise at maximum amplification, gain 10, is noisy enough that the data begins to be unreliable and tells us less about the sample.

The final source of error in the electronic recording circuit I will discuss is the A/D converter. When very small measurements are made such as in a beam current measurement or dark current measurement (see 3.3.2.3 and 3.3.2.1), the discrete nature of the digital signal becomes very obvious in the data. An example of this is in Figure 3.8 where the data points are forced into lines according to the digital spacing. Each of these sources of uncertainty contribute to the systematic error of our model and will be discussed in Section 3.4.4.

## 3.3 Data normalization

### 3.3.1 Raw data

I would like to give a few examples of what the data looks like before the normalization process. The computer is able to record a maximum signal of 10 volts, so an excessively large amplification (gain) would not be useable. At the same time, if the gain is not large enough, digitization becomes a serious issue. As such, we usually are forced to change the gain within in the run. Figure 3.4 is an example of the raw voltages we recorded at a single wavelength. In Figure 3.5 is the same data with

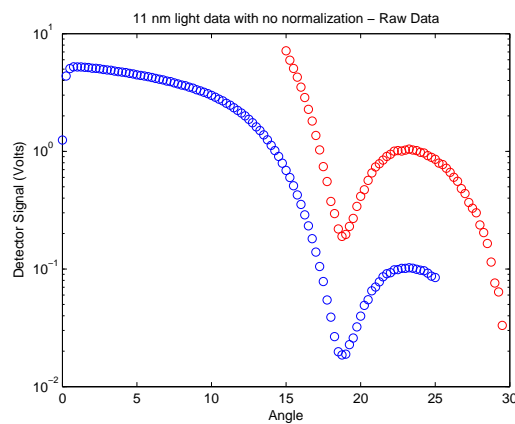


Figure 3.4: Voltage is plotted versus angle in this example of raw, completely unnormalized data. The log plot allows the low angle features to be more visible. Notice that the red curve is approximately 10x larger than the blue curve as it is one gain level higher (10 vs. 9).

the second curve divided by a factor of 10 to compensate for the amplification difference. It also shows an enlarged portion of the overlap region where ideally they should be exact. The consistently higher red curve indicates this is likely a systematic error rather than purely statistical.

### 3.3.2 Measurements

The normalization process is how we take the measured data, a voltage induced on the detector, into a measure of actual reflectance. There are four measurements used in the process:

1. detector signal
2. dark current

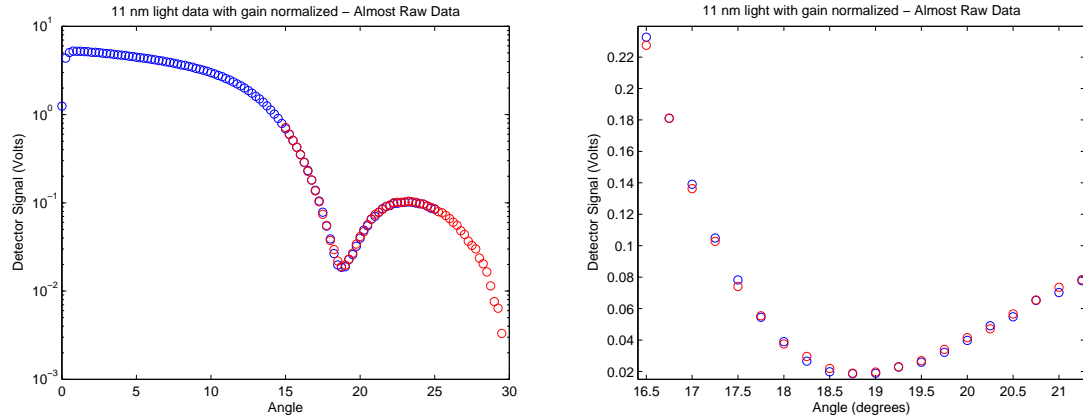


Figure 3.5: This is identical data to Figure 3.4 with the second (red) curve divided by ten to account for the amplification. The enlarged portion shows evidence that there is a systematic error when we switch from one gain to another.

3. initial intensity ( $I_0$ )
4. beam current

As I have described the data process previously in section 3.2.2, I will explain the other three measurements below.

### 3.3.2.1 Dark Current

When data is taken, not all of the signal the detector feeds to the computer is due to the incident light reflecting off the sample and hitting the detector. Errant electric fields in the environment, induction loops, and other forms of interference can cause a signal to be detected even when the incident light is turned off or blocked completely. While this signal is small compared to reflectance near grazing, it becomes very important when measuring reflectance near normal incidence.

Dark current has also been one of the more difficult errors to correct for. Taking dark current readings at various times has shown that it has the tendency to drift with time. To compensate for this, we took a new dark current reading for each data run to get as close to the instantaneous error as possible. Even with this approach, the drift with time can still cause a systematic error in our data. Additionally, the setting of the gain can have a major impact on both the size and variation within a dark current run. We took separate dark currents for each gain used in the data run and normalized each data set with a dark current of the same gain. Even with these precautions, dark

current remains a major concern when looking at systematic error sources in our data.

The procedure for dark current measurements involves blocking the incoming beam with an EUV-opaque filter such as glass, and repeating the angle scan which we used to take the measurement. This gives us as close to identical conditions as possible to the original data run, including the movement of motors and wires, to see how much of our signal is noise (see Figure 3.6).

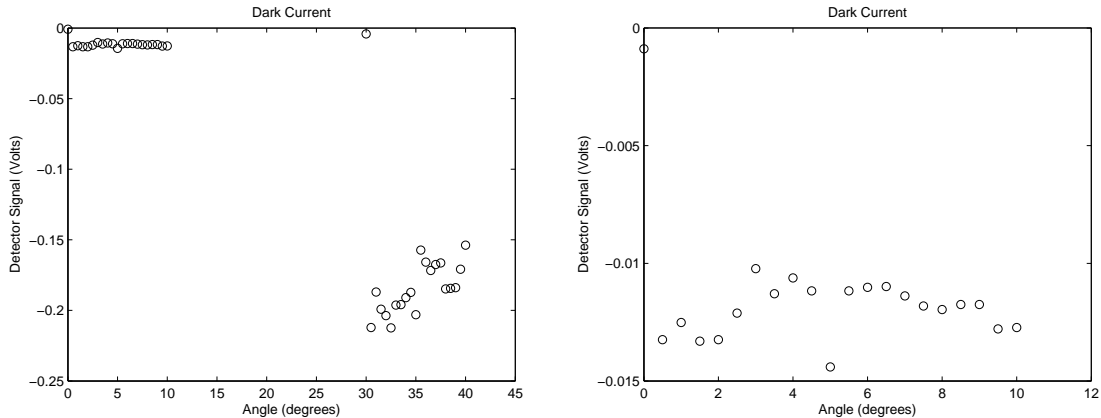


Figure 3.6: On the left are examples of two dark current readings taken less than a minute apart and at different gains. Notice the small magnitude and random pattern. Many of the runs contain negative voltages like those pictured here but this is not ubiquitous. The right image shows an enlargement of the data in the upper left of the left image showing the random nature present there too. The bottom right data within the left image is taken at a gain of 10 and demonstrates a slight trend. Also notice that the dark current changed by more than a factor of 10 when the gain went from 9 to 10. This suggests that the error is within the amplifier.

### 3.3.2.2 Initial intensity ( $I_0$ )

Since we want to know what percentage of light reflects off of the mirror at different angles, we need to know how much light was present at the start. To do this, we take a separate reading where we move the mirror completely out of the line of the incoming beam, and the lay detector flat so as to allow the entire beam to contact it. We take this measurement at each wavelength since the intensity is partially dependent on the wavelength of the incoming light, as is the sensitivity of the detector (see Figure 3.7).

### 3.3.2.3 Beam Current

The beam current is a measure of the intensity of the beam coming out of the synchrotron. It is measured directly from the current in the storage ring using a loop of wire with known inductance



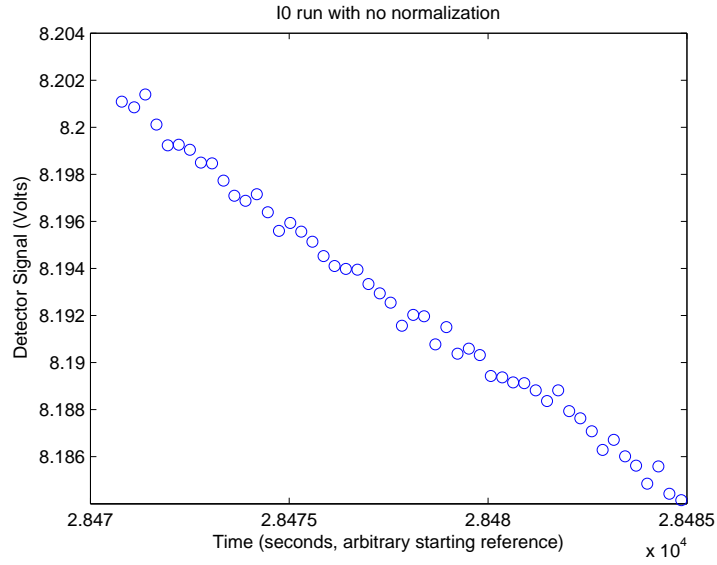


Figure 3.7: An example of an unnormalized  $I_0$  reading. The y-axis shows voltage while the x-axis is shows an arbitrary time scale. Notice the large magnitude and the gradual shift downward due to the diminishing beam current.

and measuring the induced voltage. This allows us to account for the decay of the synchrotron beam with time. Since the intensity of the synchrotron light is directly proportional to the beam current, a drop in beam current corresponds to fewer photons reflecting off of the sample (see Figure 3.8).

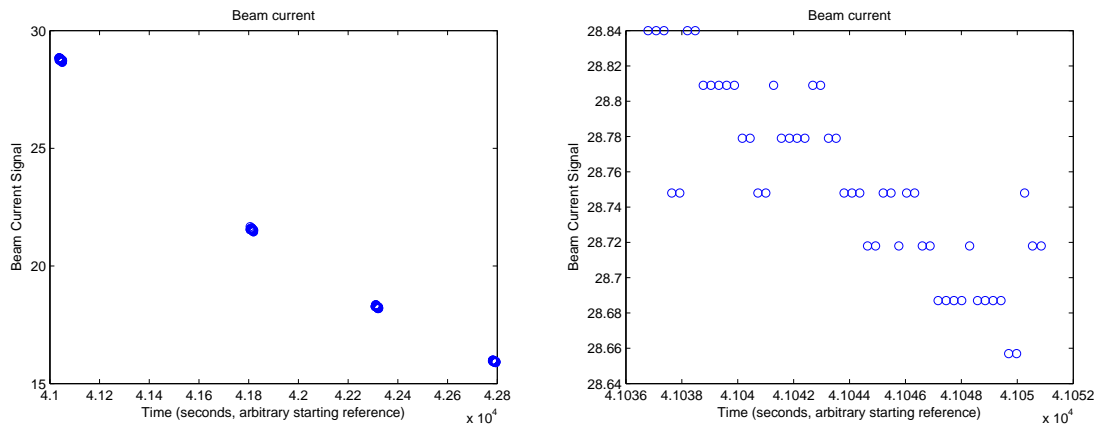


Figure 3.8: The left image shows an example of a beam current measurement taken over a five hour period. Notice the gradual decrease intensity which corresponds to the decrease in intensity in Figure 3.7. The right image shows the beam current over 16 seconds shows the discretization of an analog to digital converter. The gradual decline is evident even on this much smaller time scale.

### 3.3.3 Analysis

The process of normalization is how we take a raw voltage and convert it into the percentage reflectance that we have measured at each wavelength. The process uses the four measurements listed above along with the gain setting. First the dark currents data runs are averaged. The decision to average the dark current is a result of looking at various dark runs to determine the best way to account for the long term drift. We have noticed that while many dark runs show predictably random behavior like that pictured in Figure 3.6, some demonstrate a general trend of increasing or decreasing. We experimented with fitting the dark data linearly and using this fit in the subtraction shown below, but after considering the continued drift and the likelihood of such a trend continuing, we decided that such fit would potentially introduce new sources of error. Also considered was subtracting the dark current point by point from the data run. However, due to the random nature of the dark current at each point, this was also seen as a new source of error.

We subtract the averaged dark current from the  $I_0$  and the data. As the dark current has been taken at the same gain as the other corresponding signal, we can divide this subtraction by the amplification factor,  $10^{\text{Gain}}$  as follows:

$$D = \frac{(D_{\text{raw}} - B_{\text{mean}})}{10^{G_D}} \quad (3.1)$$

$$I = \frac{(I_{0\text{raw}} - B_{\text{mean}})}{10^{G_{I_0}}} \quad (3.2)$$

In these equations,  $D_{\text{raw}}$  refers to the actual data taken,  $I_{0\text{raw}}$  is the actual  $I_0$  data,  $B_{\text{mean}}$  is the averaged dark current, and  $G_D$  and  $G_{I_0}$  are the gain setting for the data and  $I_0$  runs respectively.  $D$  and  $I$  now represent the data and  $I_0$  runs with the dark current subtracted and adjusted for amplification. These numbers are then divided by the beam current that was measured concurrently with the data or  $I_0$  run, giving:

$$D_{BC} = \frac{D}{J_D} \quad (3.3)$$

$$I_{BC} = \frac{I}{J_{I_0}} \quad (3.4)$$

Here,  $J_D$  and  $J_{I_0}$  refer to the beam current data taken along with the data and  $I_0$  runs respectively. Finally, with a data run and  $I_0$  run that have been adjusted for dark current, gain amplification, and beam current, we divide the data by the average of  $I_0$  ( $\bar{I}_{BC} = \text{mean}(I_{BC})$ ) and we get the final

normalized data ( $N$ ) as follows:

$$N = \frac{D_{BC}}{\bar{I}_{BC}} \quad (3.5)$$

This formula yields data that behaves as we would expect it to. For instance, at 0 degrees when the beam should be passing uninhibited over the mirror, we should always have a value of one corresponding to 100% reflection. This is indeed the case for our data (see normalized data in Figure 3.9). Also, to see this formula as it was used in my code, see Section A.3.

## 3.4 Fitting

### 3.4.1 Model of Film

The model used to fit the data included four layers: vacuum,  $Y_2O_3$ ,  $SiO_2$ , and Si.  $SiO_2$  is known to exist as a thin layer (approximately 1.8 nm thick) on the surface of bare Si wafers. This was included as a separate layer for fitting purposes. The index of refraction for  $SiO_2$  and Si are taken from [5, 17] and are read using the code in Section A.8.

The surface of the  $Y_2O_3$  was modeled as a rough surface using the Debye-Waller roughness correction. The correction factor is

$$s = e^{-2q_z^2\sigma^2} \quad (3.6)$$

where

$$q_z = \frac{2\pi \sin \theta}{\lambda} \quad (3.7)$$

with  $\theta$  measured from grazing and  $\sigma$  is the RMS roughness of the surface. This correction factor  $s$  is multiplied by the reflection coefficients (Equations 2.6 and 2.7) and the transmission coefficients (Equations 2.8 and 2.9) of the Parratt formula (Equation 2.11.) This changes the Parratt formula as follows:

$$R'_2 = \frac{C_2^4(r_{21}s + R'_1s^2)}{1 + r_{21}R'_1s} \quad (3.8)$$

This adjustment is reflected in the code in `parratt.m` (Section A.1) where  $s$  is referred to as ‘eta’ to differentiate from ‘S’.

### 3.4.2 Fitting Procedure

Reflection curves become useful when we can use them to extract the optical constants for the material. This is accomplished by using a computer to try different values of optical constants and thicknesses of the thin film layer to find the optical constants that most closely match the normalized reflectance curve measured. I used a program written in MatLab by Steven Turley to accomplish this task.

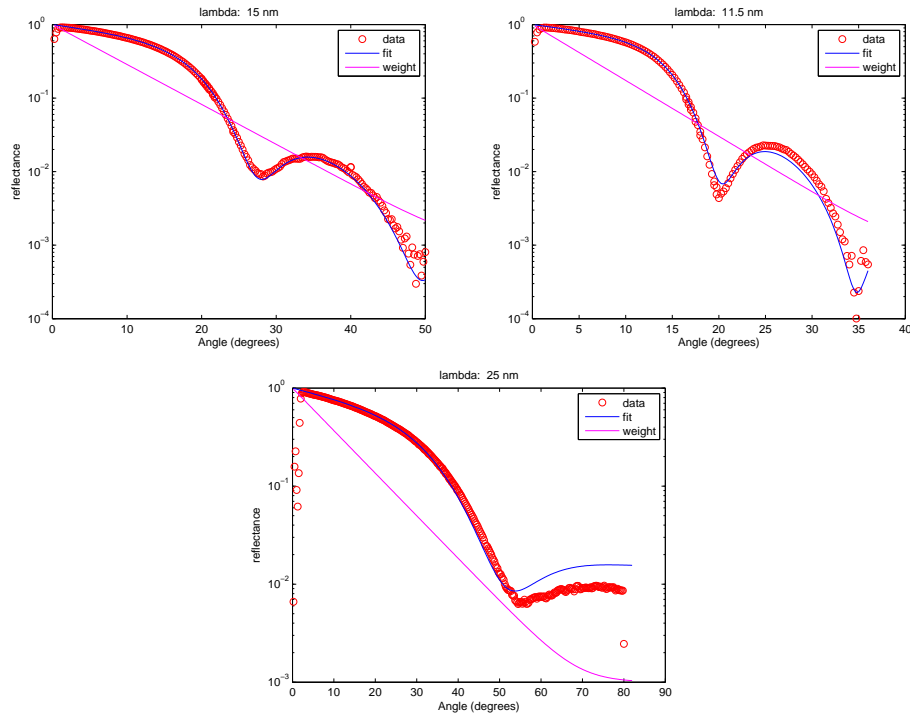


Figure 3.9: Examples of normalized reflection data, calculated fit, and the weight function used. The left is an example of a good fit, the right is a typical fit, and the lower example is one of the poorest fits. It stands out as a particularly bad fit in my final results (Figures 3.11 and 3.12)

We used a weighted least squares analysis method for fitting the normalized data. The fitting algorithm then minimized the following function:

$$\sum_{i=1}^N \left[ \frac{y_i - R(\theta, n(\lambda), d)}{e^{-\alpha\theta_i} + \sigma} \right]^2 \quad (3.9)$$

where  $y_i$  are the measured data,  $R$  is the calculated reflection using the Parratt formula (see Equation 2.11),  $N$  is the total number of data points in the set,  $\theta_i$  are the measurement angles,  $\alpha$  is a weighting constant,  $\sigma$  is a baseline noise factor (an estimate of the maximum noise at higher angles),  $n(\lambda)$  is the index of refraction (both real and imaginary parts),  $\lambda$  is the wavelength, and  $d$  is the thickness

of the sample.

From a coding aspect, this formula is used within the MatLab routine “nlinfit”. We used this function as it is able to simultaneously calculate the standard deviation as part of the covariance matrix. This is shown in the code found in Section A.3.

The denominator served as the weighting function. By using a decaying exponential, we ensured that the denominator was smallest when the data was smallest. This meant that a small variation in the theoretical fit at high angles would increase the overall summation by more than a similar variation at low angles. This was preferable since the low signal/high angle region is where much of distinguishing features caused by the optical constants is present. (see Figure 3.9)

The first objective was to determine thickness (see 3.4.3). Once I had settled on a reliable thickness measurement, the program varied the real and imaginary components of  $n(\lambda)$  until it minimized the entire summation. It then recorded the values of  $n$  and  $k$  that were found to minimize Equation 3.9.

### 3.4.3 Determining Thickness

The Parratt formula (Equation 2.11) uses several factors to determine the theoretical curve used in the fit of our data. One of those factors is the thickness of the thin film. In preliminary analysis of our  $\text{Y}_2\text{O}_3$  sample using ellipsometry, we found that the thickness was close to 20 nm. However, the model (the approximation used for the variation of the index of refraction with wavelength) used during ellipsometry had not been used previously. Since the model was untested, we were skeptical of the results. When we began fitting it became clear that we needed greater confidence and precision in our thickness measurement as small variations significantly affected the fit. To gain this precision, we decided to use our fitting program to fit both the optical constants and the thickness as separate parameters. I selected nine of the best fits and plotted the results, along with the average value (see Figure 3.10).

The results of this fit showed us that 20.5 nm was an accurate measurement of our sample thickness. The standard deviation we measured ( $\sigma = 2.96 \text{ \AA}$ ) made us confident in the result. We did note, however, the trend which is evident in Figure 3.10 (the data points are not randomly distributed about the mean). This is likely caused by systematic error. In addition to the potential sources of error discussed in Sections 3.2.2 and 3.3.3, it is possible that there is an error in the way we modeled the film. The Parratt formula assumes a sharp interface between materials and it is

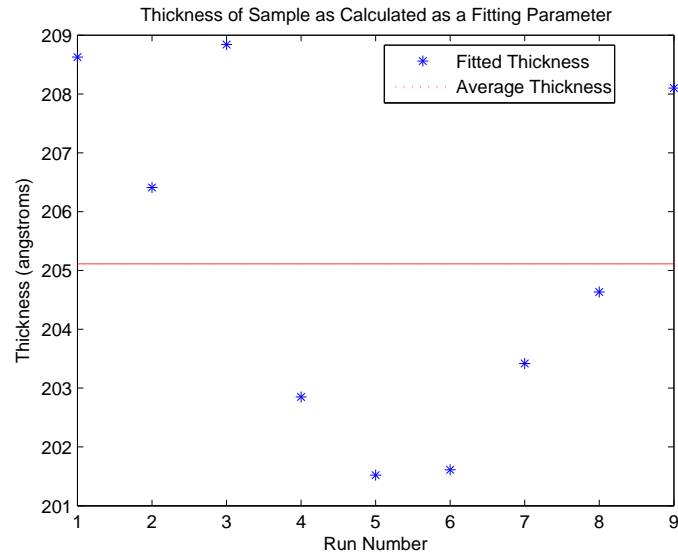


Figure 3.10: Results of nine data fits where thickness was also fit as an independent variable and the average of the nine measurements.

possible that our silicon dioxide and yttrium oxide layers interdiffused during the evaporation or thermal treatment stages of preparation. Also, it is possible that the thickness of the sample is not uniform across the surface which would mean that near grazing the enlarged beam spot would be reflected differently at different parts of the spot. The sample may have also formed a thin layer of carbon and organic matter on the surface which could act as an additional layer in the multilayer system. The substrate also has a potential oxide layer which could add yet another unaccounted for layer.

Roughness is also a potential source of this systematic error. The AFM data taken by Anthony Willey (see Section 3.1.3) indicated that the RMS roughness was about 0.64 nm. The effect of roughness is to scatter the light and is  $\lambda$  dependent. The model used here makes correction for roughness using the Debye-Waller technique. There is evidence (see [13]) that this correction is still not completely accurate, and so roughness is still a possible candidate for the observed systematic error in Figure 3.10. Please see [12, 13, 14] for a more complete description and analysis of the effects of roughness in the EUV.

### 3.4.4 Fitting results and error analysis

With the thickness determined, I fit the real ( $n$ ) and imaginary ( $k$ ) parts of the index of refraction to each data set as described above. The results are presented in Figure 3.11 and Figure 3.12 respectively. The results are close to the approximations given by the CXRO (see Section 2.3), though the results do reveal several areas where there is appreciable deviation from the theoretical calculation, most notably between 15 nm and 20 nm in the imaginary part of the index.

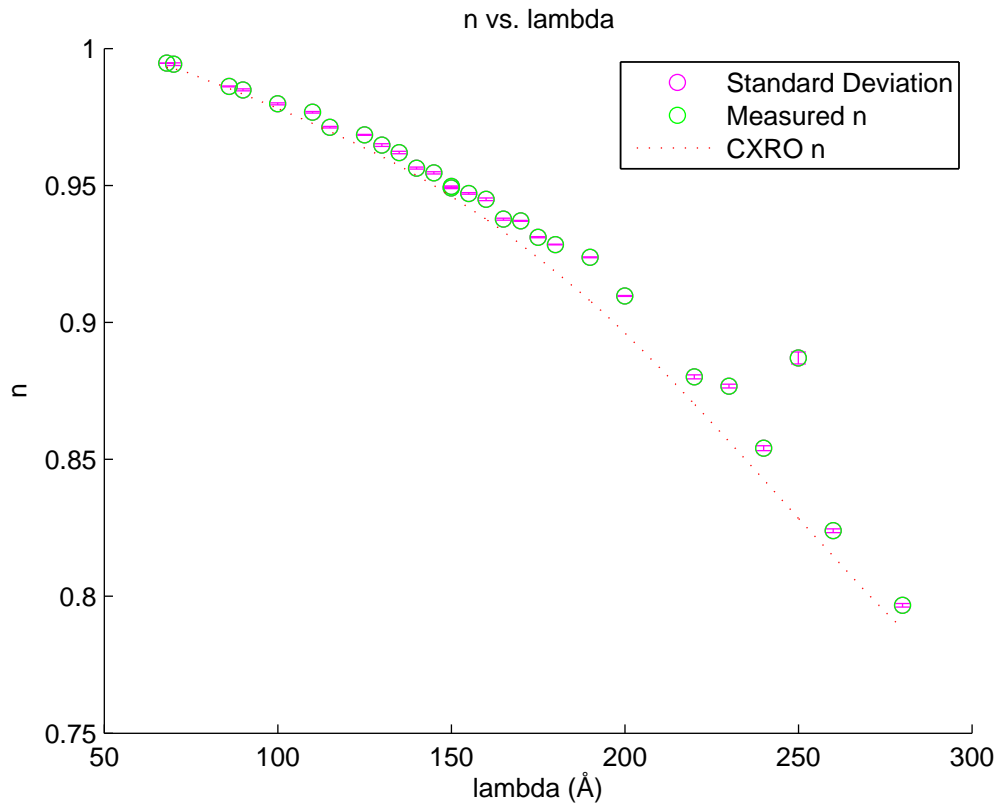


Figure 3.11: Real part of the index of refraction plotted against the data given by the CXRO.

The error bars presented here were calculated using a Monte-Carlo method. The MatLab fitting routine ‘nlinfit,’ which was also used to do the least squares analysis discussed in Section 3.4.2, returns the mean square error (mse) of the residuals. This mse was used to add noise to the data by adding a Gaussian error to each point (see Section A.7) and the noisy data was then fit. This was repeated sixteen times and the standard deviation of the sixteen fits is shown as the error bars.

This standard deviation represents the statistical or random error ( $\sigma_r$ ) which contributes to the overall uncertainty. This is one component of the overall standard deviation ( $\sigma$ ), the other being the systematic error ( $\sigma_s$ ). Assuming that the systematic error does not affect the amount of random

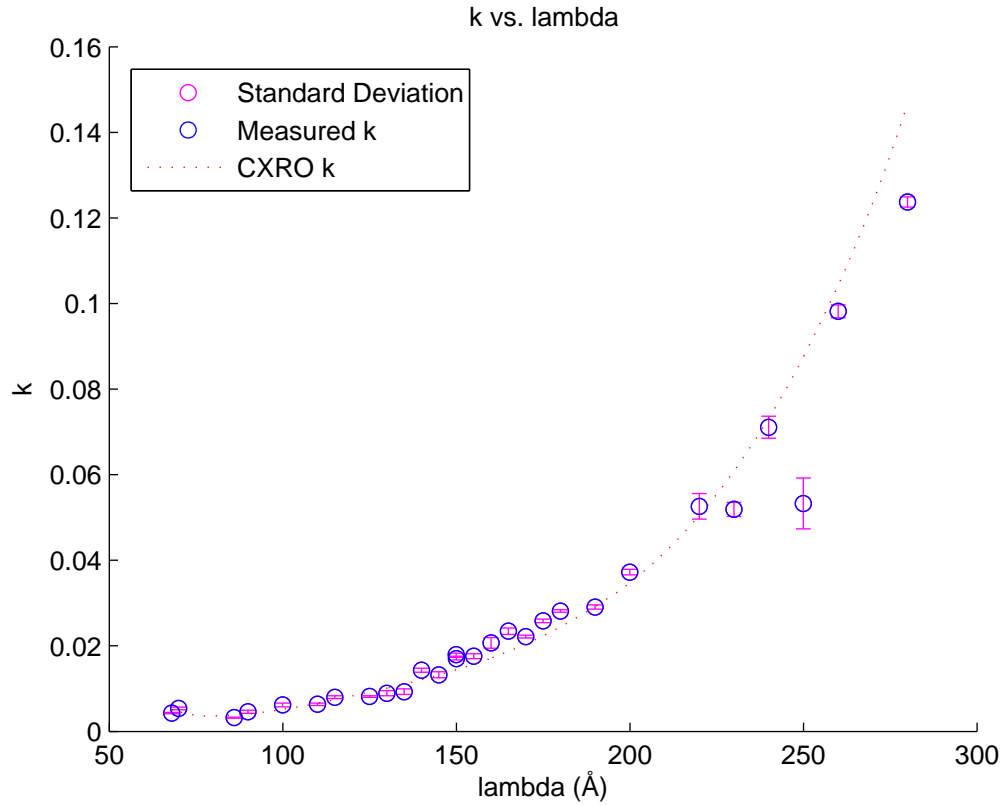


Figure 3.12: Imaginary part of the index of refraction plotted against the data given by the CXRO.

error in the measurements, a fair assumption for most of the sources of systematic error we have discussed, then the two types of error can be seen as independent of each other. Thinking of these two types of error as vectors in error-space (see Figure 3.13), the total error is the magnitude of the sum of these two error-vectors. Using the Pythagorean theorem we can deduce that:

$$\sigma = (\sigma_s^2 + \sigma_r^2)^{\frac{1}{2}} \quad (3.10)$$

As this only represents the statistical variation in the error, it is clear that it underestimates the total error of the function. As of yet, we have not found an effective method for quantifying the statistical error ( $\sigma_s$ ).



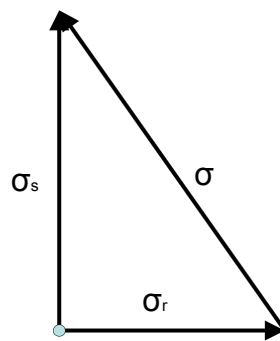


Figure 3.13: A visualization of the various components of error in error-space.

## Chapter 4

# Conclusions

Our analysis of  $\text{Y}_2\text{O}_3$  has shown that it is an excellent candidate for use as reflective material in the extreme ultraviolet. We have shown that the index of refraction used by Lunt and Turley [16] is very close to the experimental value we have measured. The maximum difference measured in  $n$  is less than .01 while the maximum difference measured in  $k$  is less than .006. This also indicates that the approximation used by CXRO that ignores the chemical bonding energy and treats the compound as a proportional mixture of atomic yttrium and oxygen is reasonable within this energy regime. Sufficient difference, however, was shown to warrant the use of the experimentally determined index. There is still concern though with the data we collected above 25 nm.

Several advantageous properties of  $\text{Y}_2\text{O}_3$  are also evident from the data. First, around 30 nm, the value of  $k$  becomes quite large while  $n$  is quite small. This is desirable when designing mirrors as there is a greater difference at the interface to cause reflection (think of the rope reflecting back when it changes thickness). Equations 2.6 and 2.7 simplify to  $\frac{n_i - n_t}{n_i + n_t}$  at normal incidence and make it immediately clear that a larger difference between the two materials will increase reflectance.

Below about 15 nm, the values of  $n$  and  $k$  both approach the values of vacuum which could make it a good spacer material at that wavelength. Additionally,  $\text{Y}_2\text{O}_3$  is an extremely stable compound, more so than other oxides yet studied in the EUV such as  $\text{SiO}_2$ . This stability makes it an excellent choice as a protective layer for mirrors made with more unstable materials.

Kramers-Kronig analysis, which uses the values of  $n$  over an extended wavelength range to find  $k$ , can now be done for  $\text{Y}_2\text{O}_3$  with greater certainty (see [18]). This analysis can be compared with the experimentally determined values of  $k$  as further verification of the data.

Characterization of  $\text{Y}_2\text{O}_3$  is still needed at additional wavelengths used by Lunt in her mirror.

Specifically, 58.4 nm needs to be studied as it is close to an absorption region where the atomic scattering factor method employed by CXRO is least valid.

The confirmation of  $\text{Y}_2\text{O}_3$ 's optical qualities in the EUV provide evidence that oxides can be useful materials for designing mirrors in the region. Their exceptional stability make them an ideal choice for mirrors that must be transported after fabrication or that will be difficult to maintain. Additionally, we have shown that  $\text{Y}_2\text{O}_3$  in particular can go through a vigorous annealing process and remain stable physically and optically. This suggests a possible way of cleaning or purifying oxides after deposition.

Electron beam evaporation has proven a possible method for  $\text{Y}_2\text{O}_3$  deposition on the  $\text{SiO}_2$  wafer when used in combination with extensive baking to remove impurities. AFM analysis has shown an RMS roughness of 6.4 Å. Future work is needed to determine if this method can be extended to use in a multilayer stack similar to the one designed by Lunt and Turley. Allred also successfully deposited  $\text{Y}_2\text{O}_3$  on a sample via sputtering. While the sputtered sample showed greater roughness than the evaporated one (3.21 Å RMS roughness), it is a more likely candidate for use in a multilayer as it does not require the extensive heating of the evaporated sample.

# Appendix A

## MatLab Code

### A.1 parratt.m

This is the code which utilizes the Parratt formula (Equation 2.11). Notice also the Fresnel coefficients for reflection (Equations 2.6 and 2.7) called “rs” and “rp”.

```
function R=Parratt(n,x,theta,fractions,lambda,sigma)
% calculate the reflectance a multilayer stack
% Written by Steve Turley, 6 July 2006
fractionp=1-fractions; % fraction of p-polarized light
S=sqrt(n.^2-cosd(theta)^2);
k=2*pi/lambda;
C=exp(i*2*S.*x*k);
rs=0;
rp=0;
qz=k*sind(theta);
eta=exp(-2*qz^2*sigma.^2); %Debye-Waller roughness correction
for m=length(n)-1:-1:1;
    fs = (S(m)-S(m+1))/(S(m)+S(m+1));
    fp = (n(m+1)^2*S(m)-n(m)^2*S(m+1))/(n(m+1)^2*S(m)+n(m)^2*S(m+1));
    rs=C(m)*(fs*eta(m)+rs*eta(m)^2)/(1+fs*rs*eta(m));
    rp=C(m)*(fp*eta(m)+rp*eta(m)^2)/(1+fp*rp*eta(m));
end
```

```

R=(fractionp*abs(rp)^2+fractions*abs(rs)^2);
return;function R=Parratt(n,x,theta ,fractions ,lambda)
% calculate the reflectance a multilayer stack
% Written by Steve Turley , 6 July 2006
fractionp=1-fractions; % fraction of p-polarized light
S=sqrt (n.^2-cosd (theta )^2);
k=2*pi/lambda;
C=exp (i*2*S.*x*k);
rs=0;
rp=0;
for m=length(n)-1:-1:1;
    fs = (S(m)-S(m+1))/(S(m)+S(m+1));
    fp = (n(m+1)^2*S(m)-n(m)^2*S(m+1))/(n(m+1)^2*S(m)+n(m)^2*S(m+1));
    rs=C(m)*( fs+rs)/(1+fs*rs);
    rp=C(m)*( fp+rp)/(1+fp*rp);
end
R=(fractionp*abs(rp)^2+fractions*abs(rs)^2);
return;

```

## A.2 fitfunc.m

This function, when given an index of refraction “b” and a list of angles (contained within “angle”) will return the calculated. Note that this function calls Parratt.m. It also assumes the thickness is 210 Å as defined in the variable “x”. This variable “x” was used as a fitting parameter when obtaining the data found in Section 3.4.3.

```

function yhat = fitfunc(b, angle ,lam)
% compute expected R given the fit parameters b
%
% For this version , I'll assume the layer thickness is known
% and I'll fit the real and imaginary parts of the index of refraction
si=sindx(lam);

```

```

sio2=sio2ndx(lam);
%y2o3=y2o3ndx(lam);
n = [1,b(1)+b(2)*1i , sio2 , si ];
x = [0,205,18,0];
sigma = [6,0,0,0];
fractions=polarfind(lam);
yhat = zeros(size(angle));
for i=1:length(angle)
    yhat(i)=Parratt(n,x,angle(i),fractions ,lam ,sigma );
end

```

### A.3 analyzer4.m

Analyzer4.m contains the code used to call the data in from the file, read the log file for such data as gain and time, normalize the data, combine various runs taken at the same wavelength but different gain, fit the combined data, and store the final data in a “a4” and “fitted4”. There is an almost identical script called analyzer5.m which performs the same function but draws data from the directory “080805”.

This first section reads in the data.

```

% analyzer.m
%Make sure that all Sample Runs are of the same wavelength
%Steven Turley and Joseph Muhlestein 2008-9

directory = '080804\';
base = '080804';
suffix = '.log';
filename = [directory base suffix];
global datafile comment date time gain scantype grating filter1 ...
    filter2 mono sample detector samplex sampley samplez lam
rsum(filename);
[ang diode m3 current] = rdat(directory);

```

The next section enters a loop which will normalize, combine, and fit all runs listed in “runner4” which is created in filler4.m. It then normalizes the data as described by Equation 3.5.

```
% Get data on a specific run
for j=4:4%length(runner4)
    for i=1:length(runner4{j})

        lambda=round(mono(runner4{1}(1))*10);

%Compute the signal-dark current with beam current normalization
        top=((diode{runner4{j}(i)} / 10^gain(runner4{j}(i)))...
        - (mean(diode{darker4{j}(i)})/10^gain(darker4{j}(i))))...
        ./current{runner4{j}(i)};
        bottom=((diode{I0er4{j}(i)} / 10^gain(I0er4{j}(i)))...
        - (mean(diode{darker4{j}(i)})/10^gain(darker4{j}(i))))...
        ./current{I0er4{j}(i)};

        %use top and bottom to compute normalized reflectance
        refl{runner4{j}(i)}=top/mean(bottom);

% figure
% plot(ang{runner4{j}(i)}, refl{runner4{j}(i)});
% xlabel('angle , degrees ');
% ylabel('Reflectance ');
% title(['Normalized Reflectance at ' num2str(mono(runn{j}(i))*10)...
% ' Angstroms ']);
end
```

This final section of analyzer4.m combines the normalized data, and then fits the data using nlinfit. This procedure follows Equation 3.9 and uses fitfunc1.m as the source of calculated data. The rest of the script stores the calculated fits and exits the loop.

```
if length(runner4{j})>1
    angle1=ang{runner4{j}(1)};
    normed1=refl{runner4{j}(1)};
    for i=1:length(runner4{j})-1
```

```

        angle1=vertcat (angle1 ,ang{runner4{j}(i+1)});
        normed1=vertcat (normed1 , refl {runner4{j}(i+1)});
    end
else
    angle1=ang{runner4{j}(1)};
    normed1=refl {runner4{j}(1)};
end

[angle , normed] = ordered (angle1 , normed1 ,1);

% Plot the data , fit , and wgt
wgt=sqrt (exp(-weight (j)*angle)+1e-6);
lam=mono(runner4{j}(1))*10;

% Initial guess for Re(n) and Im(n), and d
b0 = [(1-0.149655089), 0.0746402293, 210];
% b=fminsearch (@(b)lsq (b, angle , normed , wgt , lam), b0);
[b,r,J,COVB,mse] = nlinfit (angle ,normed ./ wgt ...
,@(x, angle) fitfunc1 (x, angle) ./ wgt, b0);

a4(1,j)=b(1);
a4(2,j)=b(2);
a4(3,j)=210;
a4(4,j)=lam;
[stdn4(j),stdk4(j)]=mocastd (angle , normed , lam , wgt , mse , b0);

fit = fitfunc (b, angle , lam);
fitted4 {1,j}=fit ;
fitted4 {2,j}=angle ;
fitted4 {3,j}=normed;
fitted4 {4,j}=wgt;
fitted4 {5,j}=lam;

```



```

figure
semilogy(angle, normed, 'ro', angle, fit, 'b-', angle, wgt, 'm-');
xlabel('Angle (degrees)');
ylabel('reflectance');
title(['lambda: ' num2str(round(lam)/10) ' nm']);
end

```

## A.4 filler4.m

This script assigns the appropriate run-numbers to be used in analyzer4.m. There is a similar script called filler5.m which corresponds to the directory 080805.

```

% fill run
t=1;%10
runner4{t}(1)=97;darker4{t}(1)=101;I0er4{t}(1)=102;
runner4{t}(2)=98;darker4{t}(2)=100;I0er4{t}(2)=102;
runner4{t}(3)=99;darker4{t}(3)=100;I0er4{t}(3)=102;
weight(t)=.4;
t=t+1;%8.6
runner4{t}(1)=90;darker4{t}(1)=94;I0er4{t}(1)=96;
runner4{t}(2)=91;darker4{t}(2)=93;I0er4{t}(2)=96;
runner4{t}(3)=92;darker4{t}(3)=93;I0er4{t}(3)=96;
weight(t)=.45;
t=t+1;%14
runner4{t}(1)=129;darker4{t}(1)=134;I0er4{t}(1)=136;
runner4{t}(2)=130;darker4{t}(2)=133;I0er4{t}(2)=136;
runner4{t}(3)=131;darker4{t}(3)=133;I0er4{t}(3)=136;
runner4{t}(4)=132;darker4{t}(4)=133;I0er4{t}(4)=136;
weight(t)=.25;

```

(Continued similarly for the rest of the runs to be analyzed.)

## A.5 combiner.m

Combiner.m calls filler4.m, analyzer4.m, filler5.m, and analyzer5.m and combines the two runs into a single data set. It then plots the calculated index of refraction on separate plots for the real and imaginary parts along with the corresponding data from CXRO which is loaded manually into “data”.

```
%combine 80804 and 80805
%Joseph Muhlestein
%10-13-08

% use to do everthing all at once
filler4;
analyzer4;
filler5;
analyzer5;

a=horzcat(a4,a5);
fitted=horzcat(fitted4,fitted5);

stdn=horzcat(stdn4,stdn5);
stdk=horzcat(stdk4,stdk5);

%test with CXRO
cxrolam=min(a(4,:)).1:max(a(4,:));
cxron=real(y2o3ndx(cxrolam));
cxrok=imag(y2o3ndx(cxrolam));

figure
hold on
errorbar(a(4,:),a(1,:),stdn,'mo')
plot(a(4,:),a(1,:),'go',cxrolam,cxron,'r:')
hold off
```

```

title('n vs. lambda')%?
xlabel('lambda Å()')
ylabel('n')
legend('Standard Deviation', 'Measured n', 'CXRO n')
figure
hold on
errorbar(a(4,:),a(2,:),stdk,'mo')
plot(a(4,:),a(2,:),'bo',cxrolam,cxrok,'r:')
hold off
title('k vs. lambda')
xlabel('lambda Å()')
ylabel('k')
legend('Standard Deviation', 'Measured k', 'CXRO k')

```

## A.6 polarfind.m

Polarfind.m takes a given wavelength and returns the corresponding polarization of the ALS synchrotron using data taken from a graph supplied by Eric Gullikson.

```

%take a lambda (in Angstroms) and return the corresponding polarization
%of the ALS (Beamline 6.3.2)
%Theoretical data on polarization from the synchrotron and verified by
%actual polarization measurements, provided by private communication from
%Eric Gullikson
function f = polarfind(lam)
% x=[10,30,100,400,800,1000];
% y=[.935,.875,.79,.67,.659,.66];
load PE.txt;
x=PE(:,1);
y=PE(:,2);
xx=1:.1:3;
yy=interp1(log10(x),y,xx,'spline');

```

```

xxx=10.^xx;
% semilogx(xxx,yy)
ev=12400/lam;
p=interp1(xxx,yy,ev,'spline');
f=(p+1)/2;

```

## A.7 mocastd.m

Mocastd.m adds a Gaussian error to the data according to the mean standard error. This is done sixteen times and the data is fit each time. The standard deviation of the sixteen fits is calculated and returned.

```

%find standard deviation based on a montecarlo simulation
function [stdn,stdk] = mocastd(angle,normed,lam,wgt,mse,b0)

iter=16;

for i=1:iter
    [b,r,J] = nlinfit(angle,normed./wgt+...
        random('norm',0,sqrt(mse),size(normed)),...
        @(x,angle) fitfunc(x,angle,lam)./wgt,b0);
    ni(i)=b(1);
    ki(i)=b(2);
end
stdn=std(ni);
stdk=std(ki);

```

## A.8 sindx.m sio2ndx.m y2o3.m

This routine references data in [5, 17] to give optical constants for Si. Spline interpolation allows points in between actual data to be referenced as well. Similar routines exist to reference data for

SiO<sub>2</sub> and Y<sub>2</sub>O<sub>3</sub> called sio2ndx.m and y2o3.m respectively.

```
function n=sindx(lambdai)
% return index of Si at the given wavelength lambdai in nm
directory='data\';
material='Si ';
postfix='.nk';
file=[directory material postfix];
% display(sprintf('opening file %s',file))
[lambda n beta] = textread(file,'%f %f %f',...
    'headerlines',8);
if(lambdai<lambda(1))
    display('WARNING: lambdai<lambda(1) in sindx')
end
% display(sprintf('%d wavelengths',size(lambda,1)))
if(lambdai>lambda(size(lambda,1)))
    display('WARNING lambdai>lambda(MAX) in sindx')
end
nd=interp1(lambda, n, lambdai,'spline');
b=interp1(lambda, beta, lambdai, 'spline');
n=nd+b*1i;
```

# Bibliography

- [1] J. Peatross and M. Ware, Physics of Light and Optics, Fall Semester 2008 (Brigham Young University, 2008).
- [2] "Dispersion prism." Wikimedia Commons. Wikimedia Foundation. 07 Feb. 2009 <[http://commons.wikimedia.org/wiki/File:Dispersion\\_prism.jpg](http://commons.wikimedia.org/wiki/File:Dispersion_prism.jpg)>.
- [3] "Layered Mirror Reflectivity." Center for X-Ray Optics. Lawrence Berkeley National Laboratory. 05 Feb. 2009 <[http://henke.lbl.gov/optical\\_constants/layer2.html](http://henke.lbl.gov/optical_constants/layer2.html)>.
- [4] "X-Ray Interaction with Matter Tutorial." Center for X-Ray Optics. Lawrence Berkeley National Laboratory. 06 Feb. 2009 <[http://henke.lbl.gov/optical\\_constants/intro.html](http://henke.lbl.gov/optical_constants/intro.html)>.
- [5] B.L. Henke, E.M. Gullikson, and J.C. Davis, X-ray interactions: photoabsorption, scattering, transmission, and reflection at E=50-30000 eV, Z=1-92, Atomic Data and Nuclear Data Tables **54** no.2, 181-342 (July 1993).
- [6] Lunt, Shannon. The Use of Genetic Algorithms in Multilayer Mirror Optimization. Thesis. Brigham Young University, 1999. Provo: Brigham Young University, 1999.
- [7] Parratt, L. G. "Surface Study of Solids by Total Reflection of X-Rays." Physical Review 95 (1954): 359-69. <[http://prola.aps.org/pdf/PR/v95/i2/p359\\_1](http://prola.aps.org/pdf/PR/v95/i2/p359_1)>. Physical Review Online Archive. 3 Feb. 2009.
- [8] "Electromagnetic Spectrum." Wikimedia Commons. Wikimedia Foundation. 05 Feb. 2009 <<http://commons.wikimedia.org/wiki/File:Electromagnetic-Spectrum.png>>.
- [9] "ALS Quick Facts." Advanced Light Source. Lawrence Berkeley National Laboratory. 05 Feb. 2009 <<http://www.als.lbl.gov/als/aboutals/alsquickfacts.html>>.
- [10] "Beamline 6.3.2." Advanced Light Source. Lawrence Berkeley National Laboratory. 06 Feb. 2009 <<http://www.als.lbl.gov/als/techspecs/bl6.3.2.html>>.

- [11] Underwood, J. H., E. M. Gullikson, M. Koike, P. J. Batson, P. E. Denham, K. D. Franck, R. E. Tackaberry, and W. F. Steele. "Calibration and standards beamline 6.3.2 at the Advanced Light Source." Rev. Sci. Instrum. 67 (1996): 1-5. American Institute of Physics. 5 Feb. 2009 <<http://www-cxro.lbl.gov/metrology/pubs/beamline.pdf>>.
- [12] Johnson, Jedediah. Computationally Modeling the Effects of Surface Roughness on Soft X-Ray Multilayer Reflectors. Thesis. Brigham Young University, 2006. Provo: Brigham Young University, 2006.
- [13] Doughty, W. Todd. Roughness Correction Model For Reflection From Perfectly Conducting Scatterers. Thesis. Brigham Young University, 2008. Provo: Brigham Young University, 2008.
- [14] Farnsworth, Nicole. Thorium-Based Mirrors in the Extreme Ultraviolet. Thesis. Brigham Young University, 2005. Provo: Brigham Young University, 2005.
- [15] De Boor, Carl. A Practical Guide to Splines. New York: Springer, 1994.
- [16] Lunt, Shannon, R. Steven Turley, and David D. Allred. "Design of Bifunctional XUV Multilayer Mirrors Using a Genetic Algorithm." J. X-Ray Science and Technology 9 (2001): 1-11.
- [17] Palik, Edward D. Handbook of Optical Constants of Solids III (Handbook of Optical Constants of Solids). New York: Academic P, 1997.
- [18] Jackson, Jacqueline. Determining The Refractive Index Of Scandium Oxide In The Euv Using Kramers-Kronig. Thesis. Brigham Young University, 2007. Provo: Brigham Young University, 2007.